TUM

SCHOOL OF COMPUTATION, INFORMATION AND TECHNOLOGY - INFORMATICS

TECHNICAL UNIVERSITY OF MUNICH

Master's Thesis in Robotics, Cognition, Intelligence

Optical Characterisation of Telecommunication-Wavelength Quantum Dots

B. Sc. Paul Kohl

SCHOOL OF COMPUTATION, INFORMATION AND TECHNOLOGY - INFORMATICS

TECHNICAL UNIVERSITY OF MUNICH

Master's Thesis in Robotics, Cognition, Intelligence

Optical Characterisation of Telecommunication-Wavelength Quantum Dots

Optische Charakterisierung von im Wellenlängenbereich der Telekommunikation emittierenden Quantenpunkten

Supervisor	Prof. Dr. rer. nat. Kai Müller
	Chair of Quantum Electronics and Computer Engineering (QEC)
Advisor	Prof. Dr. rer. nat. Kai Müller
Author	B. Sc. Paul Kohl
Submission Date	15.04.2023

I confirm that this master's thesis in robotics, cognition, intelligence is my own work and I have documented all sources and material used.

Munich, 15.04.2023   B. Sc. Paul Kohl

Acknowledgments

Abstract

Specific current classical cryptography is vulnerable to quantum algorithms run on quantum computers with exponentially scaling state space. This may be mitigated via information theoretically secure encryption in conjunction with physically secure Quantum Key Distribution (QKD). Quantum light would be an elegant choice of Quantum Bit (qubit) due to high coherence times and low absorption in commercial fibre optics. One of the most important Single-Photon Sources (SPSs) is probably the Quantum Dot (QD), which features deterministic, high rate photon generation, but one needs emissions in the telecommunication C-band (1530 nm - 1565 nm) to leverage the global minimum of absorption in standard optical fibres and in the O-band (1260 nm - 1360 nm) to leverage minimal wavepacket dispersion in the fibres. Thus, an experimental setup for Micro-Photoluminescence (μPL) measurements was built to investigate single $InAs$ QDs on $GaAs$ substrate with graded $In_{1-x}Ga_xAs$ Metamorphic-Buffer Layer (MBL) and Distributed Bragg Reflector (DBR) emitting in the C-band which were grown with Metal-Organic Vapor-Phase Epitaxy (MOVPE) and $InAs$ QDs on $GaAs$ substrate with graded $In_{1-x}Ga_xAs$ MBL emitting in the O-band grown via Molecular Beam Epitaxy (MBE). Power dependent and polarisation dependent measurements were performed with the setup on both types of samples to identify and characterise excitonic transitions and emissions were investigated w.r.t. biexciton-exciton cascades, their Fine Structure Splitting (FSS) and Degree of Linear Polarisation (DOLP). We were able to identify different excitonic transitions on both types of samples via power dependency of transitions and polarisation dependent photon energies in biexciton-exciton cascades and lack thereof in trionic transitions. We quantified FSSs of $\sim 21\,\mu eV$ and DOLPs in the range from $\sim 5\,\%$ to $\sim 18\,\%$ on the sample emitting in the C-band, on the sample emitting in the O-band FSSs as little as $\sim 21\,\mu eV$ and DOLPs from $\sim 16\,\%$ to $\sim 35\,\%$. Furthermore we examined s-shell and p-shell states of QDs from the sample emitting in the O-band and compared them to each other. In addition, we also performed comparative measurements on ensemble emissions from the sample emitting in the O-band with and without hemispherical Solid Immersion Lenses (SILs) of diameters $25\,\mu m$, $50\,\mu m$, $100\,\mu m$, and $200\,\mu m$ to improve the collection efficiency. The SILs with refractive index $\sim 1{,}52$ were fabricated via 3D lithography and their collection efficiency was simulated for different Numerical Apertures (NAs). For the NA of the used objective the collection efficiency without SILs was calculated to be $\sim 1{,}25\,\%$ and $\sim 3{,}25\,\%$ to $\sim 3{,}5\,\%$ for hemispherical SILs. The relative performance improvement of different SIL diameters was maximal for a diameter of $50\,\mu m$ with a relative performance of $\sim 146\,\%$ w.r.t. the average of reference measurements.

Contents

1 Introduction

The beginning of recorded history was marked - as the name implies - by the conception of writing and thus the ability of humankind to record information for later use. The desire to communicate securely followed shortly after, be it in a military context or any other. This lead to the invention of concepts like steganography and cryptography (at least dating back to the scytale). That is, on the one hand concealing the existence of a message and concealing its content on the other. Cryptography was also a big factor for the invention of computers, when i.a. Alan Turing used one of the first computers[1] solely for cryptanalysis. This often marks the beginnings of the information age.

1.1 Information Theory

Scientifically the newly devised computers sparked much interest in the subject matter of information and its nature: information theory was born. In addition to Alan Turing, Claude Shannon can be considered another father of information theory[2], as he managed already in 1948 in his seminal work "A mathematical theory of communication" [2] – which can be considered a *Standardwerk* of information theory – to see the concept of entropy from an information theoretical perspective rather than only thermodynamically. It is helpful not only to characterise entropy as a "measure of disorder" in a system as it is often done. It can also be seen as a measure of "ignorance" or lack of information about the system. According to Shannon, entropy gives the minimal amount of information needed to encode a certain message or how much information we have about a system. In the case of a coin with only heads we will always know what will happen if we flip it. This means we have all information for that system an thus the (information) entropy is $0\,\mathrm{Sh}$.[3] Now, if we have a normal fair coin the probability for heads and for tails is $50\,\%$ respectively and *Shannon entropy* [3, pp.500 et seqq.][2] yields a value of $1\,\mathrm{Sh} \equiv 1\,\mathrm{bit}$. This is the maximum value for this system, i.e. the system contains $1\,\mathrm{bit}$ of information which we do not have. If we have an unfair

---

[1]Although Konrad Zuse has to be credited for the invention of the first modern computer.

[2]Shannon also can be credited to elevate cryptography to its own field in one of his landmark works "Communication theory of secrecy systems" [1].

[3]The unit Shannon with unit symbol Sh to honour Shannon is equivalent to the unit of bit, which is much more common.

coin – e.g. heads with a probability of $90\,\%$ – it is fairly certain that it will come up heads. This means, because of this additional information about the coin, the entropy decreases in comparison to the fair coin and thus assumes values between $0\,$bit and $1\,$bit. Applying this to thermodynamics yields that entropy (and in turn the direction of time itself[4]) is fundamentally about our knowledge of the microscopic states of an ensemble of (classical) particles in a macroscopic system. The fact that information entropy generalises thermodynamic entropy leads to *Landauer's principle*: erasing information means heat dissipation. For example, setting an unknown bit value to 0 is a non-invertible function, thus information is lost. Applying this to a physical system yields that this information has to go somewhere independent of the systems implementation. Ultimately this is heat dissipation if we do not transfer the information somewhere else. This exemplifies that in thermodynamics we want to look at macroscopic systems and want to predict what will statistically happen, so we purposefully neglect the states of the microscopic particles in favour of the big picture. If we look at nature with emphasis on the microscopic on the other side, we enter the field of quantum mechanics. Contrasting thermodynamics, in quantum mechanics we are constantly working with the states of microscopic systems and yet entropy can still be a valuable tool. [4]

1.2 Quantum Theory

If we look at a system from the perspective of quantum mechanics we see something interesting: despite using a different theory than thermodynamics for its description, fundamentally it again comes down to information. To understand this argument we recap the basics of quantum theory. In quantum mechanics we describe the quantum state of a system as superpositions of basis states, which are eigenstates of an observable or operator. In other words, every pure quantum state is a vector in the Hilbert space $\mathcal{H}$ of the system. $\mathcal{H}$ is a vector space which consists of points, where each point describes one state of the system. A fundamental part of quantum mechanics is *Heisenberg's uncertainty principle* [5] which gives us the knowledge that we cannot precisely measure two conjugated observables like position and momentum at the same time, because by measuring one of them we disturb the other one. This can be easily seen with the example of an atom. If we want to see[5] its position x at least one photon has to interact with the atom to confirm x. This photon will impart a delta onto the momentum p of the atom altering it in the process. This induces a modicum of uncertainty w.r.t. p if we even knew it in the first place. This gives rise to the famous formulation

$$\Delta x \cdot \Delta p \geq \frac{\hbar}{2}. \tag{1.1}$$

---

[4]Given by the 2nd law of thermodynamics we have: entropy $S \geq 0$, which can be used to define the direction of time.

[5]Which is a careful choice of words in this case, because we are assuming an optical measurement apparatus.

From this we get that there is an upper limit on the amount of information we can extract from our system, which is governed by *Planck's constant* $h \approx 6{,}626 \cdot 10^{-34}$ J s ($\hbar = \frac{h}{2\pi}$ is the reduced version of Planck's constant, sometimes called *Dirac's constant*). Quantum mechanically the full system description w.r.t. energy is given by the wave function $\Psi(t)$ of the system, which is the solution to *Schrödinger's equation*[6] which determines the dynamics of the system:

$$i\hbar \frac{d}{dt}|\Psi(t)\rangle = \hat{H}|\Psi(t)\rangle \tag{1.2}$$

where $\hat{H}$ is the Hamiltonian of the system. A measurement on the system causes the collapse of the wave function, in some sense leading to a loss of information (see also Subsection 1.3.1). This scenario recalls Landauer's principle described in Section 1.1. From this we can come back again to the argument of the fundamentality of information also in quantum mechanics. In quantum mechanics one can define the *von Neumann entropy*[7] $S := -k_B \operatorname{Tr}(\rho \ln \rho)$ with *Boltzmann's constant* $k_B \approx 1{,}381 \cdot 10^{-23} \frac{J}{K}$, density matrix $\rho := \Sigma P_i |\psi_i\rangle\langle\psi_i|$ and P_i the probability of state $|\psi_i\rangle$. This means for a pure state: $\exists\, P_i = 1$ for one state and $P_j = 0 \;\forall j \neq i$ for the others, thus $S = 0$. If we have a mixed state now, S will be higher, i.e. we have accumulated some uncertainty about the state. If we describe the whole universe by a single wave function we would have a pure state with $S = 0$, but we "trace out" almost all of it – viz. the immeasurable parts – in any practical consideration. By neglecting/"destroying" information and in combination with quantum measurement this unveils the probabilistic nature of quantum mechanics. Thus, we purposefully neglect the states of the macroscopic universe in favour of the small particles in quantum mechanics. [4]

1.3 Quantum Information Theory

By consolidating both information theory (see Section 1.1) and quantum theory (see Section 1.2) we find ourselves at the beginning of a new era: the era of quantum information theory. We will now have a look at some important concepts for quantum information, then shed some light upon its uses and projected uses in the future (Subsections 1.3.1, 1.3.2 and 1.3.3). This will lead us to photonic applications in particular (Subsection 1.3.4), where we finally enter the field of quantum optics (Subsection 1.3.5) introducing Quantum Dots (QDs) and their application to communication in the telecommunication-wavelength range.

---

[6]With Bra-Ket notation: Ket $|\Psi\rangle$ denotes a column vector/wave function and Bra $\langle\Psi|$ its complex conjugate transpose (row vector).

[7]This entropy can also be generalised to Shannon entropy.

1.3.1 Quantum Measurement

As we have seen in Section 1.2 quantum measurement is a fundamental characteristic of quantum mechanics. Again, measurement results in a collapse of the wave function. This works as follows: If we measure a state in a particular basis its state vector will be projected onto the axis of measurement with a given probability. As a concrete example, let's consider the polarisation of a single photon. The measurement could for example be done with a linear polariser and a photon detector. If the photon is linearly polarised with an angle α from the horizontal axis, its corresponding state vector is $[\cos\alpha, \sin\alpha]^T$. The probability of projecting to the horizontal axis with a horizontal polariser is then $\cos^2\alpha$ and to the vertical axis $\sin^2\alpha$ (this is the *rectilinear basis* $\{|0\rangle, |1\rangle\}$). Analogously we can measure w.r.t. the *diagonal basis* $\{|+\rangle, |-\rangle\}$ with angles of $45°$ and $135°$, respectively. Those two bases are called *conjugate*. If the projection is the same for both measurement axes we lose all information about the polarisation before the measurement. [6, 7]

1.3.2 Quantum Computers and Quantum Algorithms

The concept of a quantum computer operating on quantum mechanical principles can be traced at least to Feynman in [8]. Its information carrier is called Quantum Bit (qubit), which can be any physical construct storing information in a superposition of a predefined 0- and 1-state. Because of superposition and entanglement of qubits the state space of a quantum computer grows exponentially w.r.t. its number of qubits. This may be exploited to achieve significant speedups in problems which can be described via unitary transforms (e.g. Discrete Fourier Transformation (DFT), with its quantum mechanical equivalent Quantum Fourier Transformation (QFT) running in polynomial time [9]). Such quantum algorithms include *Shor's algorithm* [9] which may speed up prime factorisations, which is the key to the widely used *RSA* encryption [10]. This attack leads to the need for classical Post-Quantum Cryptography (PQC) on the one hand and Quantum Cryptography (QC) on the other.

1.3.3 Quantum Cryptography and Quantum Key Distribution

Most of the time QC is understood as Quantum Key Distribution (QKD), which means the distribution of a cryptographic key. [11, p.111] Using a unique random key XOR-ed with a message – the so-called *Vernam cipher* or One-Time Pad (OTP) – is an information theoretically secure way of encryption, because it would be possible to generate every possible message from the ciphertext in case of a truly random key. Exchanging such a key would be possible in a secure way protected by the laws of physics themselves via QKD

protocols like *BB84* which is based on the properties of quantum measurement [7] or *E91* based on entanglement [12]. [3]

1.3.4 Photonic Quantum Technologies

In QKD *quantum light* (cf. 2.1.1) presents itself naturally as the choice of qubit. Firstly, because of the long coherence time of photons which makes communication of keys or entanglement feasible over long distances. Secondly, representing a superposition of states in polarisation possesses unparalleled elegance: for example, when encoding 0- and 1-state of the qubit in the rectilinear basis a superposition of both can be easily imagined as some polarisation angle in between, which will behave quantum mechanically upon measurement.

1.3.5 Quantum Optics

All this leads us to the field of quantum optics, which is concentrating on photonic phenomena which can only be explained by the quantum nature of light. So only if the models constructed by *classical* or *semi-classical* theories break down and are not precise enough or incapable of explaining experimental results, we can probably find the solution to our problem in the *quantum* picture. [13] We will examine quantum optical concepts important to our experiments in Section 2.1.

Quantum Dots

For quantum optical experiments one needs a high fidelity Single-Photon Source (SPS) and one of the most important and well-known quantum optical systems is probably the QD. The QD is one of the most prolific SPSs because it features deterministic photon generation. In general QDs are also much brighter and have higher emission rates, than other sources. [14, pp.12 et seqq.] Those are the main reasons why they still remain one of the most promising SPSs to date.

Quantum Dots at Telecommunication-Wavelengths

To use QDs in QKD or QC we have to be able to preserve our qubits for as long as possible, and if we look at the common (fibre-)optical applications for inspiration it seems to be the best

choice to use QDs emitting at telecommunication wavelengths. Some research has been done into QDs at telecommunication wavelengths in the recent years. [14, 15] Furthermore, near-infrared telecommunication wavelengths are widely employed in commercial optical communication networks, making this an active area of research. With sights on applicability – $e.g.$ in future QKD systems – it would be advantageous to have well-tuned SPSs at the wavelengths most suitable for fibre-optics. Thus we chose samples for characterisation at such wavelengths. This will be discussed in more detail in 2.3.1.

2 Quantum Optics and Quantum Dots

In the following we will recapitulate important theoretical concepts of quantum optics which are used to classify different types of light, in particular quantum light. We also shed light on the most important functional aspects of QDs in general and characteristics of excitonic transitions, Fine Structure Splitting (FSS) and Degree of Linear Polarisation (DOLP) as means of characterisation. We also touch on QD growth, in specific tuning their emission wavelengths via graded Metamorphic-Buffer Layers (MBLs). Finally, we will discuss how Solid Immersion Lenses (SILs) can be utilised to improve the collection efficiency from a sample.

2.1 Theory of Quantum Optics

As alluded to before, there are generally three different types of physical theories, $\mathrm{viz.}$ *classical*, *semi-classical*, and *modern* ones. The classical theories are the most well-known ones and include *Newtonian mechanics*[1], *Lagrangian mechanics*[2], and *electrodynamics* governed by *Maxwell's equations*. In case of optics this includes *geometric optics* and *wave optics*. But those theories cannot explain certain phenomena, like famously the *photoelectric effect* for which Albert Einstein won his Nobel Prize in 1921. Thus, mainly in the beginning of the 20th century this lead to development of among others quantum mechanics. But in the beginning certain aspects were not looked at in a quantised way. So to bridge the gap to the fully quantised picture, there are the semi-classical approaches. For example in case of the photoelectric effect Einstein argued that the light needs to be quantised in order to explain the observed behaviour. Yet, in [13] Mark Fox explains that – although sending us down the right path to a fully quantised picture – the photoelectric effect can also be understood in a semi-classical setting. This is the case, because one could view atoms in a quantised way, while incoming light could still be seen as an electromagnetic wave which excites the atoms' electrons ($\mathrm{cf.}$ [13, pp.3 et seqq.]). In conclusion, there are also modern theories which can actually explain effects like quantum light ($\mathrm{cf.}$ Subsection 2.1.1) which cannot be understood (semi-)classically (yet?). The modern theories can be structured in *relativistic* (thanks to

---

[1]Accessing mechanics via considerations about forces.
[2]Accessing mechanics via considerations about energies.

Einstein for that as well) and naturally *quantum* theories. As should be obvious from the preceding discussions we are interested in the quantum theory of light, i.e. quantum optics. [13]

Quantum optical experiments have established the quantum nature of light. [13] Photon statistics are often used in order to show this. First of all, we need to know that a photon is the elementary excitation of the quantised electromagnetic field and thus the carrier particle of electromagnetic force, or simply stated the particle of light. Photon statistics is the measurement of intensities of a light source and their fluctuations. Translated to the quantum picture this means one has a look at the number of photons and their statistical distribution in the beam of a specific source. A problem with this is that photodetection is a statistical process, i.e. it could veil the real statistical behaviour of the photon beam one is looking at. How to distinguish between the two will be explained in the following: First we show how the statistical nature of a light beam emerges. Then we will show how this can be masked by the statistics of photodetection. [13, 14]

Experimentally photon statistics can be done by shining onto a detector with the light source in question and integrating (i.e. continuously summing) the signal from the sensor for a specified time interval T. With the photon flux Φ of the beam and the quantum efficiency η of the sensor this gives the average number of photons counted by the detector in T: $N(T) = \eta\Phi T$. η is simply the ratio of actually counted photons and the incident number of photons on the sensor. Φ on the other hand is the average number of photons passing through the beam's cross section per second. For a perfectly coherent monochromatic beam with wavelength λ this can also be phrased as the beam's power P divided by the photon's energy[3] $\frac{hc}{\lambda} = \hbar\omega$. This gives $\Phi = \frac{P}{\hbar\omega}$. Both Φ and $N(T)$ are averages, which means that a beam with well-defined Φ will still show photon number fluctuations at short time intervals, because $N(T)$ will be no integer for short enough T. This implies rounding to the actual number of photons per interval, as photons are per definitionem discrete and individable packages. Thus emerge the fluctuations in photon number. This in turn shows the statistical nature of the light beams. [13]

To show that this can be masked by photodetection statistics we need to know the following: there are different types of light, which may be distributed according to the *Poissonian*, *sub-Poissonian* and *super-Poissonian* distributions – more on that in Subsection 2.1.1. But suffice it to say for now, that only sub-Poissonian light needs the fully quantised picture and cannot be explained by (semi-)classical theories. It can be shown that Poissonian photon count statistics can be explained without the concept of photons. Only a probabilistic nature of generating electrons in the detector from the light beam is needed for that explanation. Thus looking at the photon count statistics from the detector does not necessarily give any information about the light beam's photon statistics. [13, pp.90-92]

---

[3]$c = 299\,792\,458\,\frac{\text{m}}{\text{s}}$ is the speed of light in a vacuum and ω the angular frequency.

There are also other factors which negatively impact our ability to distinguish between the light beam's photon statistics and the statistics of photodetection: optical losses can be modelled by a Beam Splitter (BS) with some specified transmittance-reflectance-ratio, which randomly selects photons to be reflected or transmitted according to that ratio. This random sampling reduces the overall efficiency of photon counting, but different effects have different impacts on the statistics. For example, for a sub-Poissonian beam inefficient collection optics and absorption, reflection and scattering losses in optical components degrade the photon statistics into the direction of a Poissonian distribution. Furthermore, the correlation of a beam's photon statistics with the detector's photodetection statistics is lowered by an imperfect quantum efficiency η of the detector. As a more formal definition than before, we define

$$\eta := \frac{\bar{N}}{\bar{n}} \tag{2.1}$$

where $\bar{N}$ is the average number counted by the detector and $\bar{n}$ the mean photon number hitting the detector. Then our sought-after correlation is governed by the relation between the variance of $N(T)$, which is denoted $(\Delta N)^2$ and the variance of the actual number of photons $n(T)$ per interval T, which is called $(\Delta n)^2$:

$$(\Delta N)^2 = \eta^2 (\Delta n)^2 + \eta(1-\eta)\bar{n}. \tag{2.2}$$

That means, on the one hand that we have $\Delta N = \Delta n$ for $\eta = 1$, i.e. a perfect quantum efficiency would yield a perfect one-to-one correlation of impinging photons to counted photons. For an incoming Poissonian beam with $(\Delta n)^2 = \bar{n}$ on the other hand, we would have $(\Delta N)^2 = \eta\bar{n} \equiv \bar{N} \; \forall \eta$, which implies that the counted number of photons is Poissonian. And finally, also if $\eta \ll 1$ the counted photons will be Poissonian with $(\Delta N)^2 = \eta\bar{n} \equiv \bar{N}$ for any incoming photon count distribution. [13, pp.89 et seqq.]

In summary, there are many factors which can mask the photon statistics of the beam with the statistics of photodetection. That is why it is most important to have as little optical losses as possible and a detector with a quantum efficiency η which is as high as possible. [13, p.93]

2.1.1 Types of Light

We now not only know that there are different types of light, which may be distributed according to the Poissonian, sub-Poissonian, and super-Poissonian distributions, but also that sub-Poissonian photon statistics seem to be skewed towards the Poissonian case by undesirable effects. Let's now have a more thorough discussion of the different types of light.

Poissonian Light

We already know how the photon statistics emerges and there is a proof in [13, pp.78 et seqq.] that a perfectly coherent light beam with constant intensity has Poissonian photon statistics, which we will not reiterate due to the constraints of this thesis. The Poissonian distribution looks as follows[4]:

$$\mathcal{P}(n) = \frac{\bar{n}^n}{n!} e^{-\bar{n}} \tag{2.3}$$

where $\bar{n}$ is the *mean* $\bar{n} \equiv \langle n \rangle = \sum_{n=0}^{\infty} n\mathcal{P}(n)$ and the *variance* $\mathrm{Var}[n] = \bar{n}$ at the same time. From the definition of the *standard deviation* $\sigma^2 := \mathrm{Var}[n]$ we get:

$$\boxed{\Delta n \equiv \sigma = \sqrt{\bar{n}}} . \tag{2.4}$$

The distribution applies in general to random processes that will only result in integer values, just like counting photons in a beam. And in order to distinguish between the different types of light, the standard deviation in photon number is commonly used. [13] As already mentioned a coherent source like a laser has a Poissonian distribution, which implies temporally completely unrelated emission events. [14]

Super-Poissonian Light

Super-Poissonian means that the photon number distribution is smeared out in comparison to the Poissonian case. For example, if we have classical intensity fluctuations, then we expect that the fluctuations in the photon number are also higher than in the case of constant intensity. Constant intensity yields a Poissonian statistics, consequentially classical light with time-varying intensity should have a broader – i.e. super-Poissonian distribution. Thus we would expect a higher standard deviation which defines the super-Poissonian case:

$$\boxed{\Delta n > \sqrt{\bar{n}}} . \tag{2.5}$$

Examples for this type of light include *thermal light* generated by *black-body radiation* and *partially-coherent light*[5] generated by a *discharge lamp*, therefore observing super-Poissonian statistics is not rare. It seems intuitively clear that those have super-Poissonian characteristics, because they are clearly emitting light in a way which is noisy in comparison to the coherent laser regarding their intensity and their photon number fluctuations. This is because a laser works with the principle of stimulated emission – i.e. utilising quantum mechanically sharp energy transitions as emission source – and has thus very well-defined spectral, temporal

---

[4]NB The *Gaußian statistics* that generates the *normal distribution* is the continuous equivalent of this.
[5]Also commonly referred to as *chaotic light*.

and intensity behaviours. There is also a proof for this intuition. We will look exemplary at the argumentation for thermal light in the following. [13]

Obviously thermal light utilises temperature as a driving force, which is per definitionem a macroscopic and statistical quantity determined by averaging over a multitude of particles, every single one of them with potentially different micro-state. More formally, light emitted from a hot body obeys *Planck's law*, which gives a continuous spectrum of oscillating modes. A single mode of thermal light at angular frequency ω obeys the *Bose-Einstein distribution* (for the derivation of this form of the distribution cf. [13, pp.83 et seqq.]):

$$\mathcal{P}_\omega(n) = \frac{1}{\bar{n}+1}\left(\frac{\bar{n}}{\bar{n}+1}\right)^n \tag{2.6}$$

which is much broader than the Poissonian for the same value of $\bar{n}$. Mathematically speaking, we see that the variance for this distribution is always greater than for the Poissonian, proving that we are in the super-Poissonian regime:

$$(\Delta n)^2 = \bar{n} + \bar{n}^2 > \bar{n}. \tag{2.7}$$

For N_m modes of thermal light with similar frequency this is

$$(\Delta n)^2 = \bar{n} + \frac{\bar{n}^2}{N_m} \tag{2.8}$$

which will be the Poissonian case in the limit: $\lim_{N_m\to\infty} \bar{n} + \frac{\bar{n}^2}{N_m} = \bar{n}$. In case of partially coherent light, we have classical intensity fluctuations on a time-scale determined by the coherence time. As already mentioned this will lead to bigger photon number fluctuations and thus super-Poissonian light. [13]

Sub-Poissonian Light

Sub-Poissonian light has an even narrower distribution than perfectly coherent Poissonian light:

$$\boxed{\Delta n < \sqrt{\bar{n}}} \tag{2.9}$$

thus it has no classical equivalent, because perfectly coherent light is the best one can get within the classical argumentation. Thus sub-Poissonian light may be called quantum light. But just because there is no classical counterpart, it does not mean that it is difficult to imagine how the beam has to look like in order to give rise to sub-Poissonian statistics. For example, a beam with constant time intervals Δt between each photon will do the trick. This

will lead to the photon count in timespan T to be

$$N = \left\lfloor \eta \frac{T}{\Delta t} \right\rfloor \tag{2.10}$$

which is the same for each measurement and leads to $\bar{n} = N$ and $\Delta n = 0$ which is the extremal case of the Poisson distribution, where it transitions to a *Dirac δ-distribution* [16] and as such the purest form of sub-Poissonian light. Such photon streams are called *photon number states*. The different types of sub-Poissonian light are from the spectrum of options, where the intervals between photons are not exactly the same, but still more regular than for Poissonian light. [13]

Second-Order Correlation Function

As we have seen before, photon counting statistics can be used to classify light but the statistics may be skewed in Poissonian direction by various factors. But fundamentally the interest lies in the mean photon number $\bar{n}$. Mathematically we can describe classical intensity correlations via the *second-order correlation function* $g^{(2)}(\tau)$ defined by

$$g^{(2)}(\tau) := \frac{\langle I(t)I(t+\tau)\rangle}{\langle I(t)\rangle \langle I(t+\tau)\rangle} \tag{2.11}$$

with $I(t)$ the light beam intensity at time t and angled brackets $\langle \ldots \rangle$ indicating time averages. For constant average beam intensity we have $\langle I(t)\rangle = \langle I(t+\tau)\rangle$. [13, pp.111 et seqq.] We can also see that for a fully coherent beam $I(t) = I(t+\tau)$ which leads to $g^{(2)}(\tau) = 1$ and the same is the case for $\tau \longrightarrow \infty$, where the intensities of $I(t)$ and $I(t+\tau)$ become uncorrelated. It can also be shown that for this definition the *degree of second-order coherence* $g^{(2)}(0)$ fulfils following properties for any possible time dependence: $(g^{(2)}(0) \geq 1) \wedge (g^{(2)}(0) \geq g^{(2)}(\tau))$. The photon number counted by a detector is proportional to the intensity, thus follows for the photon picture:

$$g^{(2)}(\tau) := \frac{\langle n_1(t)n_2(t+\tau)\rangle}{\langle n_1(t)\rangle \langle n_2(t+\tau)\rangle} \tag{2.12}$$

with counted photon numbers $n_i(t)$ at time t at detector i of two detectors positioned equidistantly from both outputs of a 50:50 BS. [13, pp.111 et seqq.] For constant intensity $\langle n(t)\rangle = \langle n(t+\tau)\rangle$ for any detector. And for $\tau = 0$ we get the formulation

$$\boxed{g^{(2)}(0) = \frac{\langle n(n-1)\rangle}{\langle n\rangle^2} = \frac{\langle n^2\rangle - \langle n\rangle}{\langle n\rangle^2}} \tag{2.13}$$

because a photon can be detected only at one detector. With $\langle n\rangle \equiv \bar{n}$ and the general definition of variance $\text{Var}[n] \equiv (\Delta n)^2 := \langle n^2\rangle - \langle n\rangle^2$ we can now classify different types of

light also with the $g^{(2)}(0)$. Thermal light exhibits bunching, i.e. multiple photons are detected immediately after each other. Coherent light exhibits no correlation. [14, pp.7 et seq.] For single photons impinging on the BS (e.g. sub-Poissonian SPS, $n = 1$) we have a 50% chance to hit either of the detectors, which means there cannot be a correlation of photons at $\tau = 0$ and $g^{(2)}(0) = 0$. [13, pp.111 et seqq.] The phenomenon $g^{(2)}(0) < 1$ is called antibunching, which exists in photon number states.

Comparison of Different Light

As we have seen the different types of light are distinguishable by their photon statistics and $g^{(2)}(0)$. A comparison of the different distributions with the same mean photon number can be seen in Figure 2.1. Now we will give an overview in Table 2.1 of the different types of light we encountered, paired with various metrics. [13, 14]
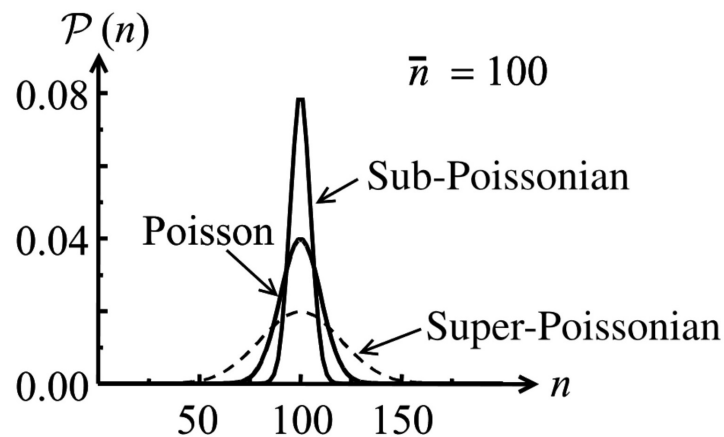

Figure 2.1: Comparison of super-Poissonian, Poissonian, and sub-Poissonian distributions for $\bar{n} = 100$. The discrete nature of the distributions is masked by the large value of $\bar{n}$. [13, p.82]

As we know Poissonian photon statistics can be explained without the concept of photons and are obtained for constant beam intensity. On the other hand varying intensity will yield super-Poissonian statistics, which may also be explained without the full quantum theory. This means, the possibility of observing a *non-classical* sub-Poissonian distribution actually shows that we need the full quantum theory to explain some experimental results. [13, pp.90-92] Sub-Poissonian distributions will also get skewed into the direction of the Poissonian

Table 2.1: Classification of different types of light. [13, p.83][14, p.8]

Type	Variance $(\Delta n)^2$	$g^{(2)}(0)$	Intensity $I(t)$	Comment
Super-Poissonian	$> \bar{n} \equiv \langle n \rangle$	> 1	$I(t) \neq const.$	e.g. light bulb
Thermal	$\langle n^2 \rangle + \langle n \rangle$	2		photon bunching
Poissonian	$= \bar{n} \equiv \langle n \rangle$	$= 1$	$I(t) = const.$	e.g. laser
Coherent	$\langle n \rangle$	1		no photon correlation
Sub-Poissonian	$< \bar{n} \equiv \langle n \rangle$	< 1	$I(t) = const.$	e.g. QDs
Photon Number	0	$1 - 1/n$		photon antibunching

(i.e. random) case by any form of loss, like optical losses and $\eta < 1$ as mentioned in Section 2.1 above. [13, p.89] Thus a more robust way to classify light also in the quantum picture is $g^{(2)}(0)$.

2.1.2 Luminescence

In order to do quantum optics and to classify the type of light coming from a system one has to stimulate a system in a way s.t. it actually emits light in the first place. To do this we must excite a quantum system's (optical) energy transitions. That means we have to excite the system in a way that elevates it from a low energy state to a higher energy state which relaxes optically, that is it emits a photon in doing so. The other possibility would be *acoustic relaxation* via emission of one or multiple phonon(s)[6]. This kind of optical relaxation is in general called *luminescence*. [13, p.60]

We still can discriminate between two different ways of exciting the system: either Electroluminescence (EL) via electrical excitation, or Photoluminescence (PL) via optical excitation on which we focus here. [13, p.60]

2.2 Theory of Quantum Dots

QDs are one of the most prolific SPSs compared to others like Spontaneous Parametric Down Conversion (SPDC) or Four Wave Mixing (FWM), which dominated quantum optical experiments in the telecom range historically. SPDC and FWM generate photons via spontaneous processes which results in uncertain photon generation times. The down conversion

---

[6]Phonons are the quanta of the elastic field, i.e. quasi-particles which arise by vibrationally exciting a crystal lattice. They are probably best described as the particle-like dispersion relation of a *Gitterschwingung* (german, lit. translates to "lattice vibration").

works via a nonlinear effect in crystals like Beta Barium Oxide (BBO) and Periodically Poled Potassium Titanyl Phosphate (PPKTP). Another detrimental factor is the thermal photon statistics, which give rise to a trade-off between pump power and efficiency. This means that it is mostly necessary to use low powers to avoid multi photon generation. This leads to low rates which is not ideal for applications like QKD. Effects due to the spontaneous nature of the emission are not present in QDs and they are also much brighter and have higher rates, thus they enjoy great popularity. [14, pp.12 et seqq.]

2.2.1 Quantum Dots, Confinement and Epitaxial Growth

In general, QDs are small structures which are made of 10^3 to 10^5 atoms, exhibiting quantum mechanical (atom-like[7]) behaviour due to the confinement of charge carriers within them. There are different kinds of QDs, e.g. semiconductor or colloidal QDs, but we concentrate on the epitaxially grown semiconductor variety here. The charge carriers are confined by creating a potential barrier for them via the difference in bandgap of different semiconductor materials. If we have a material with smaller bandgap surrounded by material with larger bandgap (see Figure 2.2a) charge carriers can be trapped in the inner material, because their wave function is spatially confined (see Figure 2.2b).
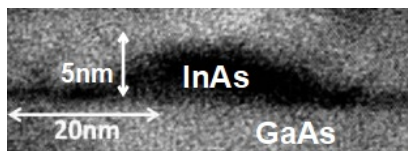
(a) Transmission Electron Microscope (TEM) Image of a QD with relevant length scales.
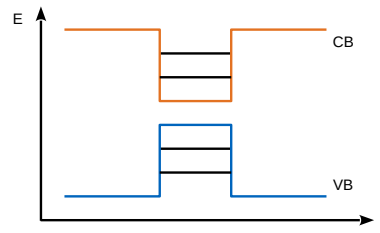
(b) Band diagram of Conduction Band (CB) and Valence Band (VB) in the QD's z-direction with discrete states.

Figure 2.2: A QD with $\sim 5\,\mathrm{nm}$ thickness in z-direction and corresponding band structure in z-direction.

Confinement in all three spatial Degrees of Freedom (DoF) yields a dot/pointlike or "0-dimensional" quantum structure – hence the name "quantum dot". A confined wave function yields quantised states with discrete energy levels. [14, pp.15 et seqq.]

---

[7]Hence QDs are also called *artificial atoms*.

To understand the energy structure of a QD we need to know about their spatial shape and examining their growth will yield insights on their shape. Epitaxial growth functions via one of three growth modes:

Volmer-Weber Growth   Where the interaction in between the adsorbate itself is stronger than between adsorbate and the surface. Thus, the deposited material will stick to itself first and creates islands. [17]

Stranski-Krastanow Growth   Where the interactions between adsorbate and surface is stronger. First one or few monolayers of the adsorbate is grown (also called Wetting Layer (WL)) and on that islands form. [18]

Frank-van der Merwe Growth   Where interaction between surface and adsorbate and intra-adsorbate are equal, thus monolayers are formed on top of each other directly. [19, 20, 21]

The QDs we use are grown via *Stranski-Krastanow*, which means that the islands of low bandgap material – which are the QDs – are created via *lattice mismatch* and in turn strain. Since the bulk material's small lattice constant does not match the relatively large lattice constant of the adsorbate material, the WL tries to match the lattice constant because it is energetically favourable. This introduces strain which will be relaxed by the formation of the islands/QDs at a certain thickness (see also Figure 2.6 and Section 2.3 for further information). This typically yields a lens shape (see Fig. 2.2a) for the QDs with higher confinement in z-direction (growth direction) than in-plane. Due to this lens shape one can approximate the confinement in z-direction as a *quantum well* (see Fig. 2.2b) with eigenvalue

$$E = \frac{\hbar^2 k^2}{2m} \tag{2.14}$$

and the Hamiltonian in x- and y-direction by a harmonic oscillator:

$$\hat{H} = \frac{\vec{p}^2}{2m} + \frac{m\omega^2}{2}(x^2 + y^2) \tag{2.15}$$

where m is the *effective mass*[8] of the charge carrier. Solving Schrödinger's equation for a

---

[8]Effective mass is a metric which describes the reaction of particles to forces, as if they had this mass, i.e. higher effective mass means slower reaction.

circular QD yields the eigenvalues

$$E_{n,l} = \hbar\omega(2n + |l| + 1) = \hbar\omega(s + 1) \qquad (2.16)$$

where $n = 0, 1, 2, ...$ is the principal quantum number and $l = \pm0, \pm1, ...$ the azimuthal quantum number. Thus, $s = 2n + |l|$ denotes the shell index (each shell with degeneracy $2(s + 1)$) in analogy to the energy structure of an atom, i.e. $s = 0$ is the *s-shell*, $s = 1$ the *p-shell* and so on. Thus, smaller QDs in general emit at higher wavelengths. The size of the QD is not arbitrarily large though. In order to influence the charge carriers through the confinement the QD has to be of the order of the *De Broglie wavelength* [22] of the carriers, i.e.

$$\lambda_{DB} = \frac{h}{\sqrt{3mk_BT}}. \qquad (2.17)$$

This reveals a temperature dependence and if the temperature is low enough – i.e. s.t. k_BT is less than the electron-hole binding energy – both electron e^- and hole h^+ are able to create the *exciton* X. X is a quasi-particle, which is able to recombine under emission of a photon. [14, pp.15 et seqq.]

2.2.2 Excitonic Quasi-Particles

The degeneracy of the s-shell is 2, i.e. there are two energy levels which can be occupied by two e^- or two h^+ with different spins respectively according to the *Pauli principle*. [14, pp.15 et seqq.] Generally there are light holes and heavy holes which have distinct effective masses, but light holes can be neglected for our purposes here, because they are not strongly coupled due to their lower effective mass and compressive tension in the QD. [23, pp.15 et seqq.] This yields the five different types of excitonic quasi-particles shown in Figure 2.3. Only the so-called *dark exciton* DX (Fig. 2.3b) is not optically active, i.e. it does not emit a photon upon recombination. All the others are more interesting for our purposes, viz. the aforementioned exciton X (Fig. 2.3a) consisting of one h^+ and e^- with opposite spin, s.t. it can recombine radiatively, the *positively charged trion* X^+ (Fig. 2.3c) and *negatively charged trion* X^- (Fig. 2.3d) made of one additional carrier[9], and finally the *biexciton* XX (Fig. 2.3e) which is the fully occupied s-shell[10]. [14, pp.15 et seqq.] The DX is not optically active because e^- has a spin of $\pm\frac{1}{2}$ and heavy holes have a projection of total angular momentum of $\pm\frac{3}{2}$, thus the DX has a consequently values of ± 2. The bright X on the other hand has thus values of ± 1 and circularly polarised light also has spin ± 1. Thus the light couples to X and not DX because of conservation of angular momentum. Due to the same reasoning it is easy to see that X^+, X^- and XX are also optically active. [23, pp.15 et seqq.] In summary

---

[9]Thus the energy is shifted w.r.t. neutral X due to the additional charge.
[10]The additional charge carrier also shifts the energy w.r.t. the other transitions here.

every (optical) transition in the s-shell emits at a distinct wavelength, which is the key to distinguish between them experimentally with different methods discussed later.
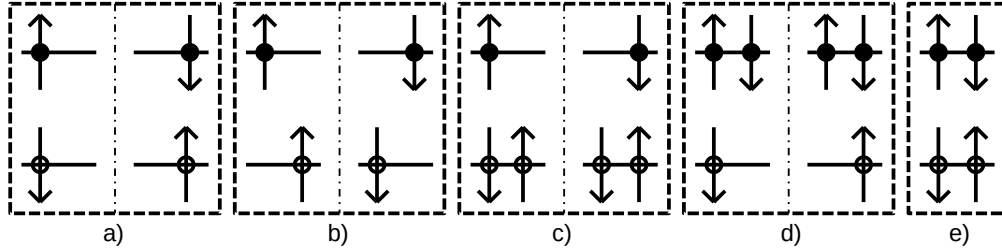

Figure 2.3: Different spin configurations for possible quasi-particles made of e^- and h^+:
   a) Excitons X b) Dark excitons DX
   c) Positive trions X^+ d) Negative trions X^-
   e) Biexciton XX
   The arrows indicate spin direction, while an empty circle depicts an h^+ and a filled circle an e^-. Adapted from [14, p.17].

Fine Structure Splitting

The biexciton decays via the exciton state. This mechanism is called *biexciton-exciton cascade* (see Fig. 2.4). It can be used for entanglement generation, because the rotational symmetry of a QD means that both bright excitons have the same energy. This means if the XX decays it emits a photon and the system is then in superposition of both bright X states (e^- up-spin, h^+ down-spin and e^- down-spin, h^+ up-spin). If they are degenerate the two paths to the ground state are indistinguishable (see Fig. 2.4a) and the system is in the entangled state

$$|\Psi\rangle = \frac{1}{\sqrt{2}}(|RL\rangle + |LR\rangle) \qquad (2.18)$$

where the emission from XX is either right circularly polarised $|R\rangle$ or left circularly polarised $|L\rangle$ and the following emission from X vice versa accordingly. But in case of anisotropic in-plane shape of QDs this leads to the so-called FSS. This effect can be seen in Figure 2.4b, which shows that the excitonic energy levels will be split by an energy difference due to different confinement in the spatial directions. This yields either biexcitonic emission in a vertically polarised photon $|V\rangle$ with different energy than the following vertically polarised excitonic emission, or a horizontally polarised biexcitonic photon $|H\rangle$ and another horizontal excitonic

one. Mathematically this can be described via the effects of the *exchange interaction*[11] with Hamiltonian

$$\hat{H}_{Exchange} = -\sum_{i=\{x,y,z\}} \left(a_i \hat{J}_{h+i} \hat{S}_{e-i} + b_i \hat{J}_{h+i}^3 \hat{S}_{e-i} \right) \tag{2.19}$$

with a_i and b_i determining the spin interaction strengths and $\hat{J}_{h+i}$, $\hat{S}_{e-i}$ spin operators along axis i. This way one can quantify the FSS. [14, p.17 et seq.] Thus large enough[12] FSS implies that the paths to the ground state from the XX are distinguishable breaking the entanglement. This means existing FSS gives us the opportunity to identify all four different emissions from XX with high certainty. If the FSS is large enough it can be resolved directly by a spectrometer. In our case the spectrometer did not consistently allow clear resolution of the FSS, thus inspecting the polarisation dependent behaviour of QD emissions could be used for this purpose. [14, pp.15 et seqq.]

(a) Biexciton-exciton cascade without FSS.

(b) Biexciton-exciton cascade with FSS.

Figure 2.4: Biexciton-exciton cascades with and without FSS. Adapted from [14, p.19].

By inspecting Figure 2.4b we get that the FSS can be calculated in principle by following formula:

$$FSS = E_{V_X} - E_{H_X} \tag{2.20}$$

with energies E_{V_X} for the vertically polarised exciton emission and E_{H_X} for the horizontally polarised exciton emission. Its sign is then an indicator if horizontal or vertical polarisation has a higher energy level. This should be completely equivalent to

$$FSS = E_{V_{XX}} - E_{H_{XX}} \tag{2.21}$$

for the biexcitonic emissions. But experimentally this may not be as clear. Thus in [24] Young et al. propose to fit the measured emission lines with *Lorentzian* (cf. also Section 2.2.3) line

---

[11] It changes the energy level of multiple identical interacting particles w.r.t. the case where the particles are not identical.

[12] I.e. if the FSS is detectable because it is larger than the linewidth of the transitions.

shapes and use

$$FSS = \frac{(E_{H_\text{x}} - E_{V_\text{x}}) + (E_{V_\text{xx}} - E_{H_\text{xx}})}{2}$$

(2.22)

to minimise systematic errors and measure the FSS accurately. This should average out some of the noise generated by the measurement setup and combat the finite resolution of the spectrometer.

Trionic States

The negative trion X^- recombines to a single e^- left in the QD. Its excited state does not show splitting of energy levels because of exchange interaction, as the two antiparallel electrons have total spin 0. The state after recombination is also not split, because exchange interaction exists only for more than one particle. Thus this transition does not have FSS. [23, pp.19 et seq.] Analogously there is no FSS between the transition of X^+ to the single hole after recombination. [23, p.21] Thus trions are simple Two-Level Systems (TLSs) and this means we can distinguish trionic states from excitonic and biexcitonic ones in polarisation dependent measurements, because trions do not exhibit polarisation dependent spectral shift due to FSS as a biexciton-exciton cascade would.

2.2.3 Linewidth and Lineshape

Atomic transitions do not produce perfectly monochromatic photons. The lineshape of the wavepacket is more akin to a *Lorentzian distribution* for *homogeneous* broadening effects. As we will see in the following some of those effects are intrinsic, so the Lorentzian constitutes a best-case scenario. *Inhomogeneous* broadening effects – which include thermal effects – result in a *Gaußian distribution*. [13, pp.56 et seqq.]

Regarding the linewidth of emissions of a QD there is a fundamental limit which generalises Heisenberg's uncertainty limit. Due to the properties of the Fourier Transform (FT) decreasing the (temporal) width of a pulse its corresponding spectral linewidth will increase. The finite lifetime of a state is governed by an exponential decay with increasing lifetime (i.e. a *Laplacian distribution*). The FT of this distribution is the Lorentzian, hence the pulses are fundamentally limited spectrally. A pulse at the lower limit is thus called *Fourier-limited* or *transform-limited*. This satisfies the uncertainty limit called *(Heisenberg-)Gabor limit*, described by the time-bandwidth frequency-bandwidth product.[13] [25] In principle a photon's wavepacket can be at

---

[13]Due to finite lifetimes of the excited state, there is some intrinsic spectral broadening as explained through the Gabor limit. Perfectly monochromatic states with Dirac δ-distribution [16] would thus imply violation of uncertainty limitations or infinite broadening in the temporal domain.

the spectral limit without dephasing (*i.e.* Lorentzian lineshape), but coupling of a QD to its surroundings can affect its linewidth. For example, phonons will have an effect on the lifetime of excitonic states which in turn has a spectral broadening effect. Dephasing thus influences the wavepacket's temporal and spectral distribution. Firstly, this will result in inhomogeneous broadening towards a Gaußian and secondly, this will degrade indistinguishability.

So the environment of a QD can have undesired effects on the emissions. This should be reduced by cooling the sample to cryogenic temperatures ($\sim 4\,\mathrm{K}$ in our case), which decreases (phononic/thermal) dephasing effects. Thus it is justified to fit bandwidth-limited peaks with a Lorentzian with minimal Full Width at Half Maximum (FWHM)[14] for cryogenic temperatures. Another way of avoiding inhomogeneous broadening effects would be a resonant excitation scheme instead of non-resonant (which we used in our experiments). This helps because it excites the transitions directly and avoids the many non-radiative relaxation processes which the charges undergo before reaching the QD energy levels. [13, pp.56 et seqq.]

2.2.4 Degree of Linear Polarisation

To investigate the polarisation properties of a system, the so-called DOLP of the photons emitted from different excitonic recombinations can be measured. It can be used as a metric to describe how much of the wave under investigation is polarised in a certain way. There are different ways of defining DOLP with some ambiguity [26], but according to Wyborski et al. DOLP is defined as

$$DOLP := \frac{(I_{max} - I_{min})}{(I_{max} + I_{min})} \tag{2.23}$$

where I_{max} and I_{min} are the maximal and minimal intensity w.r.t. polarisation of a peak under consideration. [27] Henceforth, I will use this definition and I will examine the DOLP later on in the polarisation resolved PL measurements in Chapter 4. It also has to be kept in mind that for our purposes of identifying energy transitions in the QD the DOLP has limited use and thus we will not go into much depth regarding that.

We have now established what QDs are and shown some metrics how to characterise them in principle. We will now focus on the specific samples which were used with our experimental setup (cf. Chapter 3) and what techniques were used to grow them.

---

[14]The FWHM is the general metric for quantifying the linewidth.

2.3 Quantum Dots Emitting in the Telecom Bands

In the following we will describe the samples to be characterised and how they are structured. This way we can estimate what to expect from experimental measurements and then test our hypotheses with reliable data. The samples were grown via Metal-Organic Vapor-Phase Epitaxy (MOVPE) and Molecular Beam Epitaxy (MBE), such that the QDs should emit in the wavelength ranges of the C-Band and the O-Band, which I will elaborate on in the next subsections.

2.3.1 Telecommunication Wavelengths

The electromagnetic or light spectrum is divided into spectral bands for optical and photonic applications according to the International Organization for Standardization (ISO) standard *ISO 20473:2007*. This includes the Ultraviolet (UV) radiation up to $380\,\text{nm}$, then the Visible (VIS) radiation or simply "light" from $380\,\text{nm}$ to $780\,\text{nm}$ and finally Infrared (IR) from $780\,\text{nm}$ up to $10^6\,\text{nm}$. For telecommunication in optical fibre networks generally light in the Near-Infrared (NIR) part of the electromagnetic spectrum from $780\,\text{nm}$ to $3000\,\text{nm}$ according to *ISO 20473:2007* is used. [28] This is done, because generally fibre optical networks use silica (SiO_2) fibres, which have very little attenuation in that wavelength range. The attenuation of light with wavelengths from $600\,\text{nm}$ to $1800\,\text{nm}$ in silica fibres can be seen in Figure 2.5.
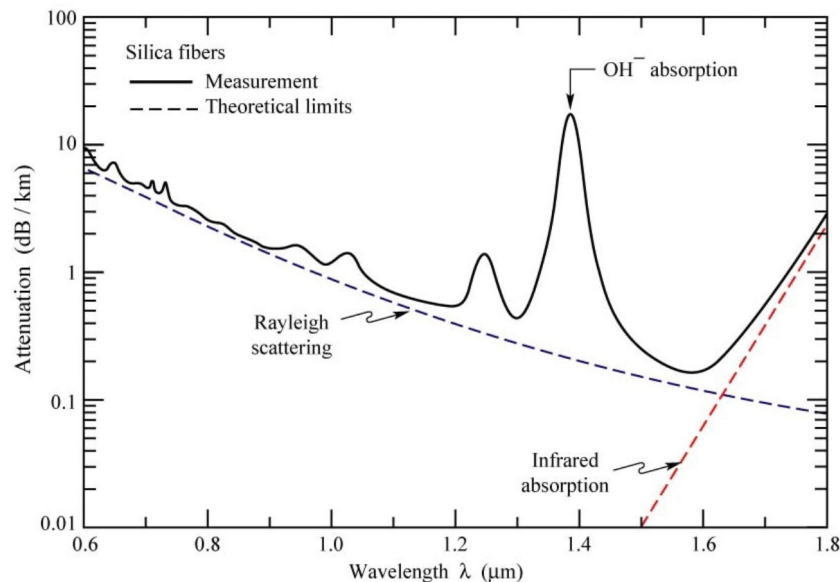

Figure 2.5: Theoretical and measured absorption in standard silica optical fibres. [29]

Historically the part of the NIR which has these desirable attenuation characteristics was subdivided into different wavelength bands with different names. A summary of the bands with their corresponding boundaries can be found in Table 2.2.

Table 2.2: Classification of infrared telecommunication bands. [30]

Shorthand	Name	Lower Bound	Upper Bound
O-Band	Original band	1260 nm	1360 nm
E-Band	Extended band	1360 nm	1460 nm
S-Band	Short band	1460 nm	1530 nm
C-Band	Conventional band	1530 nm	1565 nm
L-Band	Long band	1565 nm	1625 nm
U-Band	Ultra-Long band	1625 nm	1675 nm

There are different local minima in attenuation in those ranges, which are created by different loss mechanisms in the fibres. On the one hand, the attenuation should decrease with increasing wavelength λ due to elastical scattering on particles with diameter $d \ll \lambda$ (i.e. *Rayleigh scattering*), because the *Rayleigh scattering cross-section* is $C_{s,\lambda} \propto \frac{1}{\lambda^4}$. [31, p.460] This means, in general higher λ would be beneficial. On the other hand, with increasing λ IR is increasingly absorbed by SiO_2, which sets the upper part of the L-band and the U-band at a disadvantage compared to the C-band. There is also the big OH^- absorption peak in the regions of the E- and S-band, that set the E- and S-bands at a disadvantage compared to the O- and C-band. Thus, the lowest attenuations can be found around ~ 1310 nm and ~ 1550 nm,[15] i.e. the O-band and the C-band would be most suitable for telecommunication purposes. The losses in the O-band are higher than in the C-band but it is still used because there is zero wave packet dispersion, which leads to minimal signal distortion attributed to chromatic effects. [14, p.12][32] It has also been shown that it is possible to couple QKD and classical communication to the same fibre with Wavelength Division Multiplexing (WDM), which works best for the O-band in metropolitan area networks. [33] In summary, these are the main reason for the prominent use of O- and C-bands in fibre optical telecommunication and consequentially also a deciding factor for the fabrication of the QD samples to emit in those bands.

2.3.2 Growth of Quantum Dots Emitting in the C-Band

First we measured a sample with QDs emitting in the C-band which was grown as described in [14, pp.20 f., pp.37 ff.], because there was already data gathered in a similar setup to ours, which is not only good in order to validate the setup but also as a baseline for a comparison

---

[15]NB Nevertheless it has to be mentioned that the C-band occupies the area around the global minimum of attenuation.

with the samples with QDs emitting in the O-band which will be the main focus of this thesis.

The sample emitting in the C-band (its structure can be seen in Fig. 2.7) consists of a GaAs substrate with self-assembled InAs QDs grown on an $\mathrm{In}_{1-x}\mathrm{Ga}_x\mathrm{As}$ MBL, with $x \in [0; 0{,}6]$. GaAs substrate was used in order to be lattice-matched to an AlAs-GaAs Distributed Bragg Reflector (DBR). When InAs and GaAs are grown on top of each other they experience strain due to their rather large lattice mismatch of $\sim 7\,\%$ (see difference in lattice constant of InAs and GaAs in Figure 2.6), forming self-assembled QDs (see Section 2.2).
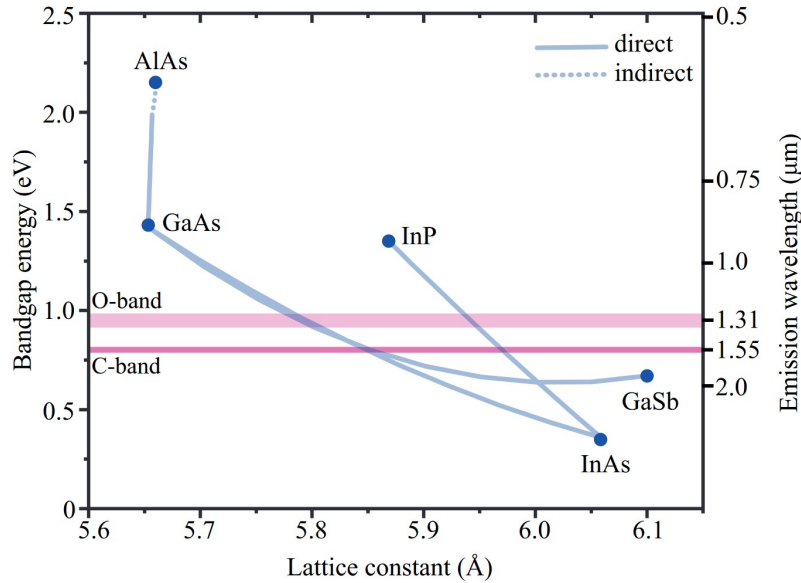

Figure 2.6: Lattice constant *vs.* emission wavelength and bandgap energy for different semiconductor compounds with emission in the telecom range. [14, p.21]

Unfortunately, according to [34] such dots would emit from an effectively increased bandgap of $900\,\mathrm{nm}$ - $950\,\mathrm{nm}$. Not just the bandgap influences the emission wavelength, but also the strain, QD size, and material composition. Thus, the growth of an MBL can be used to shift the emission wavelength to the C-band. The MBL is an $\mathrm{In}_{1-x}\mathrm{Ga}_x\mathrm{As}$ layer with increasing indium content on the GaAs to tune its lattice constant to the desired value. How the In content of the MBL affects the lattice constant can be seen as the blue line connecting GaAs ($\mathrm{In}_0\mathrm{Ga}_1\mathrm{As}$) and InAs ($\mathrm{In}_1\mathrm{Ga}_0\mathrm{As}$) in Figure 2.6. On top of the MBL InAs QDs are grown, which are now exposed to less lattice mismatch than before and consequently increase in size. [14, pp.20 et seq.] Thus, the InAs QDs are capable of emission in the C-band around $1550\,\mathrm{nm}$. The sample was grown by MOVPE, i.e. metal-organic compounds are vaporised and injected with a carrier gas into a reactor chamber, the compounds are pyrolysed and adsorbed to the wafer's surface, where they grow into a new epitaxial layer of the wafer's crystal lattice, which makes them a suitable candidate for scalable applications. Beneath the MBL the sample has a DBR grown at $670\,^\circ\mathrm{C}$. It is made of 20 layers of AlAs – each

82 nm in thickness – alternated with 20 layers of $GaAs$, which are 130 nm thick. The DBR reflects emissions from QDs in downwards direction upwards, s.t. the collection efficiency is increased, because more emission reaches an objective above the sample. The MBL is also grown at $670\,°C$. It is 1150 nm thick, and starts as In_0Ga_1As (i.e. simply $GaAs$) and its indium content is quadratically increased to $In_{0,4}Ga_{0,6}As$ at the top. On the MBL the QD layer is grown at $545\,°C$ to minimise the FSS. The sample has a 250 nm thick $In_{0,35}Ga_{0,65}As$ layer on top of the dot layer, which reduces strain in the QDs and preserves their size, thus helps preserving their emission wavelength. [14, pp.37 et seqq.]
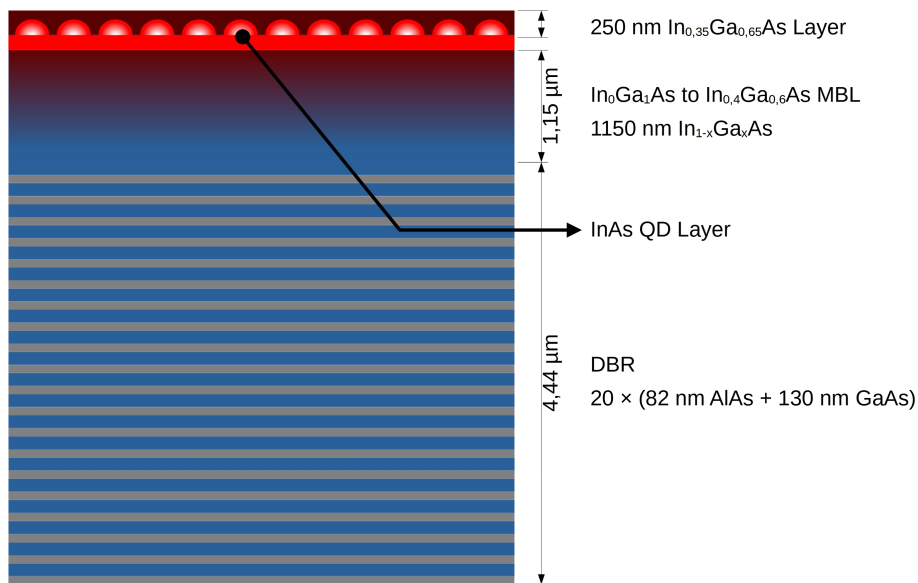

Figure 2.7: Structure of the sample with QDs emitting in the C-band.

2.3.3 Growth of Quantum Dots Emitting in the O-Band

The main focus of this work is the study of QD samples emitting in the O-band. The samples were taken from a $GaAs$ substrate wafer with QDs grown via MBE. [35] MBE growth is carried out in an Ultra-High Vacuum (UHV) via thermal vaporisation of desired materials. The vaporised materials form high-purity molecular vapour beams which impinge on the heated sample, kept at the desired growth temperature. This effects epitaxial growth on the sample. [36] As the QDs are grown via the Stranski-Krastanow growth mode we expect a non-negligible FSS, because the strain relaxation may yield non-symmetric QDs. The structure of the wafer is visible in Figure 2.8. It consist of $InAs$ QDs grown on top of an $In_{1-x}Ga_xAs$

MBL to tailor the emission wavelength towards the O-band (see Section 2.3.2 for the working principle of the MBL). First an $80\,nm$ GaAs buffer layer is grown for growth temperature calibration, then an AlAs layer of $100\,nm$ thickness – to prevent propagation of defects from the commercial substrate – followed by a GaAs layer of $34\,nm$ thickness both grown at $610\,^{\circ}C$. The MBL was grown at $450\,^{\circ}C$ with a thickness of around $700\,nm$ with increasing In content. The content was increased from $\mathrm{In_0Ga_1As}$ (i.e. GaAs) to $\mathrm{In_{0,32}Ga_{0,68}As}$ at the top, which sets the lattice mismatch for the active QD layer. To obtain a gradient in QD density on the sample – to allow single QD spectroscopy – the QD growth was carried out for the first $10\,s$ without substrate rotation followed by further $12\,s$ with substrate rotation to complete their growth. For the QD growth $2{,}4$ monolayers of InAs were deposited on the MBL at $410\,^{\circ}C$. Finally, a $100\,nm$ thick capping layer with fixed In content ($\mathrm{In_{0,18}Ga_{0,82}As}$) was grown on top of the active layer at the same temperature. [35]
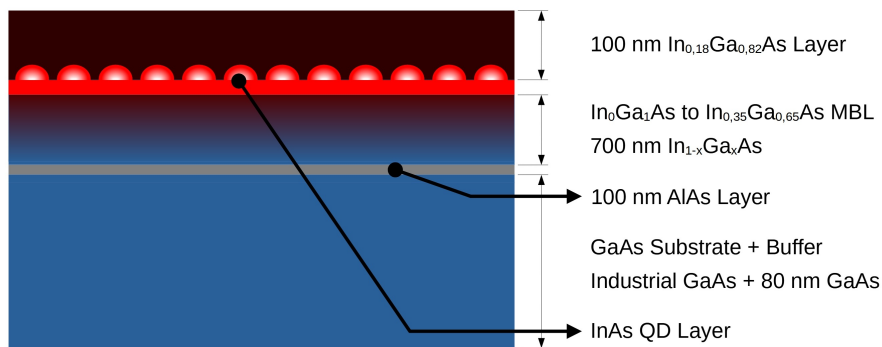

Figure 2.8: Structure of the sample with QDs emitting in the O-band.

Solid Immersion Lenses

SILs can be used as additional means of improving the collection efficiency from the sample, just as a DBR underneath the sample. In Chapter 4 we will look at a simulation of collection efficiency improvement for SILs. The last measurements we conducted were an investigation into the brightness of emissions with and without SILs. This is then compared to the expectations gained from the simulation. One sample was taken from the wafer with QDs emitting in the O-band for power and polarisation dependent Micro-Photoluminescence (µPL), another sample was used to explore the effects of SILs on the emissions. We expect an increase in collection efficiency with SILs because of their working principle which I will introduce in the following. The jump in refractive index from the sample to the surrounding vacuum in the cryostat is one of the mechanisms resulting in a lowered collection efficiency

by the objective. This is caused by total internal reflection of QD emissions at the sample surface. The higher the jump in refractive index, the lower the angle for total internal reflection, i.e. less light reaches the objective. This is governed by the equation

$$\theta_{Crit} = \arcsin\left(\frac{n_{Env}}{n_{Host}}\right) \tag{2.24}$$

where θ_{Crit} is the critical from which point on light is totally internally reflected and n_{Env} and n_{Host} are the refractive indices of the environment and the host material, respectively. A so-called SIL can be employed to decrease the total internal reflections, because it substitutes the environment with n_{Env} which is typically air or vacuum ($n_{Air} \approx n_{Vacuum} = 1$) with higher refractive index material with n_{SIL}. Thus θ_{Crit} is increased. SILs do not generally increase the outcoupling efficiency as much as specialised cavities like micropillar or bullseye cavities or planar DBRs, but they may be combined with some of them and do not require as much processing. The lens material is not the only factor playing a role here though. The other important factor is the lens geometry, which should ensure that the light hits the lens' surface at an angle, s.t. it can leave the lens without being totally internally reflected. For this purpose different geometries can be employed. The simplest geometry would probably be a hemispherical shape. Here the centre of the cut-off sphere is located on the sample surface, ideally directly over the light source. For big lenses (i.e. the radius of the SIL is much bigger than the distance of light source to sample surface) we can approximately assume that each beam exiting from the centre of the hemisphere will reach the SIL's surface in (almost) normal direction. This means that the light will not be diffracted and as such not collimated. Collimation can be achieved with a special hyperhemispherical SIL, i.e. the centre of a cut-off sphere is located above the sample surface. The collimation is due to *Weierstraß geometry*, that is the height of the hyperhemisphere h_{SIL} has to fulfil following constraint:

$$h_{SIL} = r_{SIL}\left(1 + \frac{1}{n_{SIL}}\right) \tag{2.25}$$

where r_{SIL} is the radius of the sphere. That way a beam emitted from the light source underneath the SIL at $\theta_{Crit,Host-SIL} = \arcsin(n_{SIL}/n_{Host})$ – i.e. it is running in parallel to the sample surface – hits the SIL surface at the critical angle $\theta_{Crit,SIL-Env} = \arcsin(n_{Env}/n_{SIL})$. Thus it is also diffracted s.t. it is tangential to the hyperhemisphere. This yields a collimation effect into a cone with half-angle $\theta_{Crit,SIL-Env}$ and in turn the Numerical Aperture (NA)[16] of the SIL is $NA = n_{Env}\sin(\theta_{Crit,SIL-Env}) = 1/n_{SIL}$. [37]

A 4×4 array of hemispherical SILs with varying diameters ($25\,\mu$m, $50\,\mu$m, $100\,\mu$m, and $200\,\mu$m – four of each diameter) were fabricated onto one of the samples emitting in the O-band by Björn Jonas. The SILs were fabricated from *IP-S* photoresist polymer by *nanoscribe*

---

[16]Describes the acceptance/emitting cone of an optic operating in medium with refractive index n with half-angle θ via $NA = n\sin(\theta)$.

via 3D lithography. The resist has refractive index $n_{SIL} \approx 1{,}515$ measured at $20\,°\text{C}$ at $589\,\text{nm}$. [38] In Chapter 4 we will investigate the effects of such SILs on the sample emitting in the O-band.

2.4 Characterisation of Quantum Dots

For the proper characterisation of the QDs we need to make sure that they show the desired behaviour. True single photon generation would be indicated by sub-Poissonian photon distribution and in turn by the measured degree of second-order coherence $g^{(2)}(0)$ (see Section 2.1.1), but first general properties of the QD emissions were studied.

In the next chapter the experimental setup I built in order to optically address single QDs will be described. μPL power series measurements and μPL polarisation dependent measurements with excitation above the bandgap energy were carried out for the samples with QDs emitting in the C-band and O-band in order to identify excitonic and biexcitonic states in the s-shell and p-shell and draw conclusions about the energy structure of the respective QD.

Polarisation dependent measurements allowed us to measure the FSS even smaller than the spectrometer resolution: the QDs under investigation are not necessarily symmetric in the x-y-plane. This leads to anisotropic confinement (cf. Section 2.2.1) and transitively to anisotropic emissions. The difference in confinement may result in a DOLP for different directions in the QD and can also be used as a way for measuring spectral oscillations, which are a symptom of FSS for different emitted polarisations.

Furthermore the impact of SILs on the collection efficiency of an ensemble of QDs was investigated on a sample emitting in the O-Band.

The captured data of said experiments will be presented and discussed in Chapter 4. As an outlook, the implementation of following excitation schemes can be carried out with the setup: Resonance Flourescence (RF), PL Excitation (PLE) measurements, wide field microscopy, and investigations into other collection efficiency increasing modifications of the samples[17]. Another relevant measurement would be the degree of second-order coherence $g^{(2)}(0)$ to show that the QDs on the samples are SPSs.

---

[17]For example, a DBR on the sample emitting in the O-band, with or without SILs.

3 Experimental Setup

With this chapter we turn towards the practical aspects of the characterisation of QDs at telecom wavelengths. In the following, I will introduce the setup that has been built in order to study excitonic transitions in QDs on the samples which were grown according to Section 2.3. The first experiments were done on the sample emitting in the C-band. First, we collected data regarding the DBR's reflectivity. We then perform µPL measurements with above bandgap excitation, where we conducted power series measurements and polarisation dependent measurements on different QDs on the sample. The same was also done for the sample emitting in the O-band after swapping the samples and recalibrating the setup for the other wavelength range. As the sample emitting in the O-band had no DBR yet, the measurements regarding that were omitted. In the end we also measured the impact on collection efficiency of SILs on the sample emitting in the O-band, to see if this was another viable method to increase the efficiency in addition to a DBR. I will now explain some of the considerations which lead to the design of the setup to achieve this in an efficient manner.

The setup can be divided into two parts, the PL setup which was used to generate the emissions from the sample and lead them to the second part – the spectrometer subsystem. The spectrometer subsystem is used to generate the spectroscopy data from the emission. It is connected to the PL system with a fibre connector, because it was also used in turns by another group in the same laboratory. I will explain the different parts of the system in the subsequent sections.

3.1 Photoluminescence Setup

In order to characterise QD samples emitting in the telecom C-band and O-band I built a setup for non-resonant and resonant excitation. The setup was built on an *attoDRY800* optical table [39] by *attocube* with integrated cryostat which is situated on four around $60\,\mathrm{cm}$ high *S-2000A Stabilizer* pneumatic vibration isolators with automatic re-leveling from *Newport* [40] to decouple the setup from any vibrations. The table's integrated cryostat cools the samples down to about $4\,\mathrm{K}$ to minimise thermal noise. The main part of the setup and the imaging system are situated on two bread-boards with a *cartesian grid* of M6 threaded

holes with $2{,}5\,\text{cm}$ spacing[1], which are mounted on $18\,\text{cm}$ pillars. This is done to have an easy path into the cryostat which can be accessed from above with special Anti-Reflective (AR)-coated windows. [39] The lasers for excitation are mounted on the optical table and their outputs are routed onto the bread-boards via Single-Mode Optical Fibres (SMFs) terminating in fibre couplers/collimators. To be able to tune the power of the lasers more fine-grained I constructed a fibre attenuator controller to attenuate the power via an optical attenuator (see Subsection 3.1.1). The attenuator is inserted into the fibre path in between the laser and the fibre coupler on the bread-board of the PL setup. The PL setup's beam path goes through the imaging subsystem and into the cryostat and back into the detection path in a free-space setup (cf. 3.1.2). As alluded to before, the main part of the PL setup is situated on a separate bread-board than the imaging system. This is done in order to be able to swap the PL setup for another experimental setup without the need to change the imaging system. Therefore, we have to enforce only one constraint, viz. that the excitation and detection beam paths of the different experimental setups have to exit (and enter in case of the detection path) their respective bread-boards at the same position (see Figure 3.3). Then we can simply swap them out without touching the imaging subsystem. The different modular subsystems will now be described in a sequence following the light from its source downstream.

3.1.1 Fibre Attenuator Subsystem

First we will have a look at the aforementioned fibre attenuator controller, because the attenuator is connected directly to the excitation laser via a Polarisation Maintaining (PM) SMF and is as such the first apparatus the light interacts with. The controller – henceforth abbreviated as Fibre Attenuator Box (FAB) – can control up to six fibre attenuators which may be connected in between excitation lasers and fibre couplers on the bread-board. In case of the experiments we conducted only one channel of the FAB was needed, viz. for the attenuation of the non-resonant above bandgap excitation laser at $785\,\text{nm}$. We used a PM fibre-coupled Micro-Electro-Mechanical System (MEMS)-based optical attenuator *V800PA* by *Thorlabs* [41]. But for future RF, PLE, and potentially other experiments the FAB can also control attenuators of the same kind for radiation around $1310\,\text{nm}$ ($\mathrm{e.g.}$ *Thorlabs V1000PA* [42]) and $1550\,\text{nm}$ ($\mathrm{e.g.}$ *Thorlabs V1550PA* [43]) at the same time.

Figure 3.1 shows the relation of the attenuation factor set in the FAB to the output power of the laser. The power values for the conversion of FAB attenuation factor to laser power were measured directly after coupling out of the fibre of the non-resonant excitation laser at $785\,\text{nm}$ (see Figure 3.3 for reference). The FAB attenuation factor was stepped through from value 0 to $65\,535$ with a step size of 1024. The waiting time between each measurement was $5\,\text{s}$ to let the attenuator settle in and stabilise. For simplicity we used linear steps for the attenuation

---

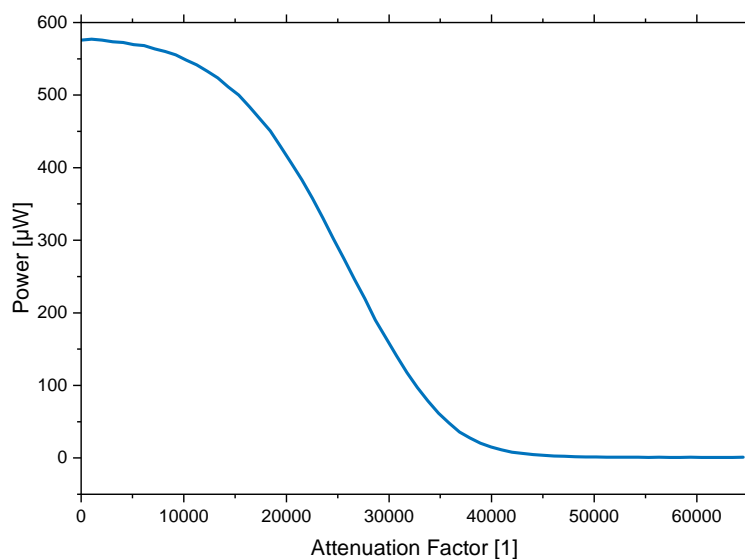[1]Spacing measured from centre point to centre point of neighbouring holes.

Figure 3.1: Relation of attenuation factor to output power of the FAB.

factor. Those steps yield the relation in Fig. 3.1, i.e. in the power series measurements more (power) values in the high and low power regions are used than in the intermediary region. But this was fine for our measurements because low power measurements were more important in our case anyways. Extremely high attenuation factors result in almost complete attenuation. Thus we used the average of the last measurements where the excitation power is negligible as a noise floor for the respective measurement. The step size can be changed in software via a linear transformation, s.t. there would be a linear power stepping in the future – or any other function, which may prioritise certain power ranges and steps faster through others.

3.1.2 Free-Space Subsystem

The beams from the lasers which may or may not be attenuated are guided from the lasers onto the bread-board with PM SMFs, where they exit via a fibre coupler. From this point the beams are manipulated in a free-space setup which can be seen in Figure 3.3. The legend to understand the pictograms used in the figures for the description of the setup can be found in Figure 3.2. The beams following the non-resonant excitation path (cf. Figure 3.4) and the resonant excitation path (cf. Figure 3.5) are combined with a dichroic mirror and aligned to follow the same path forward. The path is guided down into the cryostat to excite the sample. The emissions from the sample (and a backreflection of the laser) are then returning in the same path and are then either routed into the imaging subsystem (lower part of Figure 3.3)
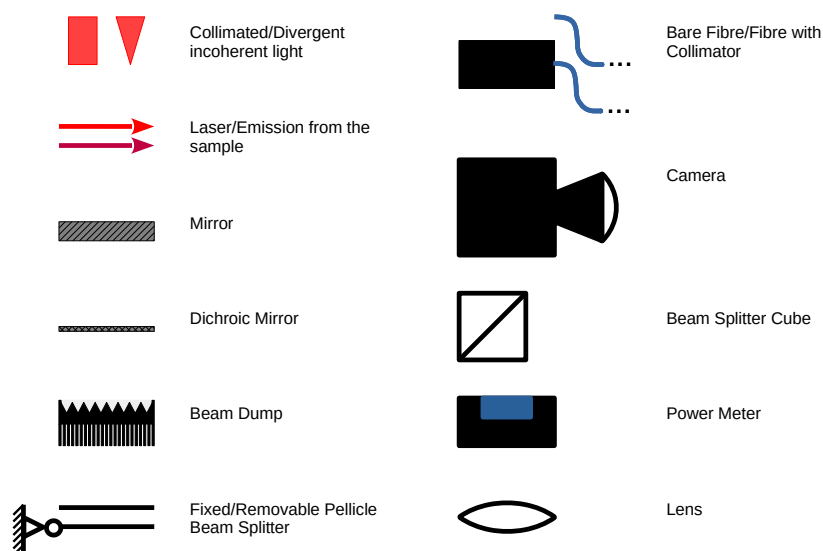
▮▼	Collimated/Divergent incoherent light	■... ■...	Bare Fibre/Fibre with Collimator
⟹	Laser/Emission from the sample	📷	Camera
▨	Mirror	◩	Beam Splitter Cube
⊡	Dichroic Mirror	▬	Power Meter
⋀⋀⋀	Beam Dump	▬	Power Meter
⊢—	Fixed/Removable Pellicle Beam Splitter	⬯	Lens

Figure 3.2: The legend for the used symbols in the optical schematics.

with a drop-in pellicle for inspection or the detection path (cf. Figure 3.9) via a BS. This is the general structure of the setup and in the following I will describe it in more detail following the path of light from the outcoupling to the detection incoupling.

Non-Resonant Excitation Path

The $785\,\text{nm}$ laser beam is guided from the laser through the fibre attenuator with PM SMFs for $780\,\text{nm}$ and ends in a *Series 60FC-SF* fibre coupler/collimator from *Schäfter+Kirchhoff* [44] on the bread-board. The coupler is mounted on the bread-board with a beam height of $75\,\text{mm}$. As can be seen in Figure 3.4 the collimated laser beam is then aligned by two mirrors in mirror mounts from *Newport* in the middle of an $45°$ angled *Thorlabs DMSP1000* dichroic mirror in yet another *Newport* mirror mount. Any possible reflections of the beam by the dichroic mirror are dumped in a beam dump, while the main beam is transmitted. From this point on the beam is coincident with the resonant excitation path discussed in the next section.
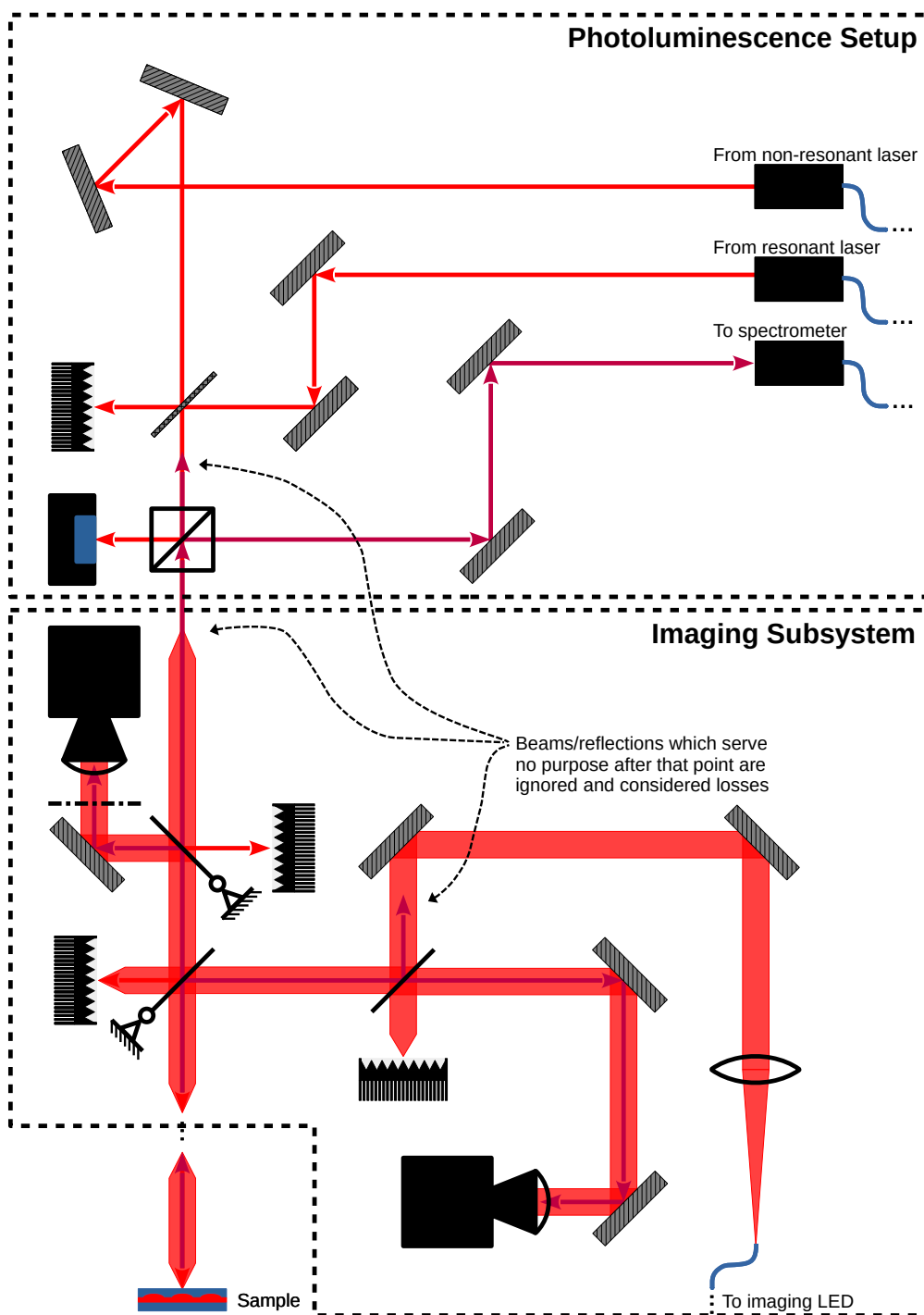
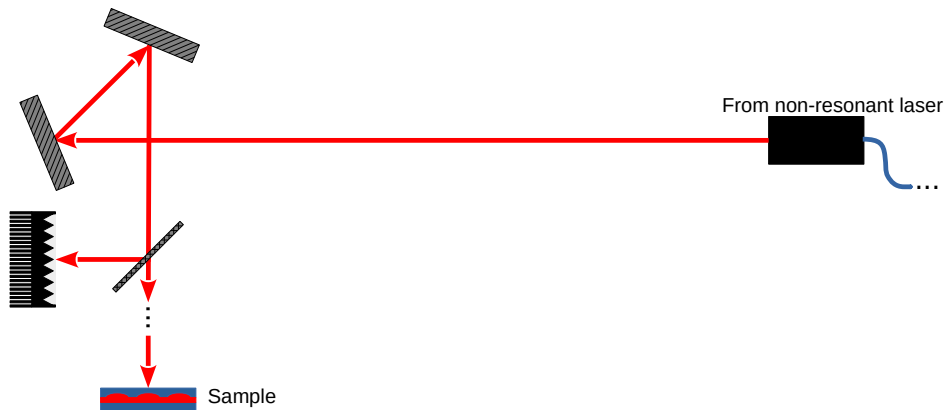Figure 3.3: The complete free-space setup without the cryostat.

Figure 3.4: The non-resonant excitation path made of the fibre coupler to the $785\,\text{nm}$ excitation laser, two mirrors and the dichroic mirror.

Resonant Excitation Path

For (future) RF and PLE experiments and coupling in at the emission wavelengths in the C- and O-band[2] we constructed the resonant excitation path. This part of the setup is analogous to the non-resonant path, but we use a *CTL 1550* and a *CTL 1320* from *Toptica Photonics* [45] for wavelengths around $1550\,\text{nm}$ and around $1310\,\text{nm}$ for the C-band and O-band radiation, respectively. Those may also be attenuated by the other channels of the FAB with a corresponding attenuator. To couple in we use a PM SMF at $1310\,\text{nm}$. The beam is then coupled out with a *Series 60FC-F* fibre coupler/collimator from *Schäfter+Kirchhoff* [46] on the bread-board. The alignment of the beam is again achieved by two mirrors in front of it. The beam was aligned, s.t. it hits the dichroic mirror in the middle but from the other side, i.e. from a $90°$ rotated position. That means, only a very small portion of its beam will be transmitted and dumped, while the larger portion of power is reflected in direction of the cryostat, coincident with the non-resonant excitation beam. This can be seen as the red path in Figure 3.5. In this figure and following ones the beam path(s) not under investigation in the corresponding section is/are greyed out to reduce clutter. After traversing this path the light hits a *Thorlabs BS066* non-polarising BS cube with $70\,\%$ reflectance [47], which is used to separate the excitation paths from the detection paths discussed later and continues to the cryostat.

---

[2]The backreflection of the C- and O-band radiation from the sample mimics the emission from the sample, s.t. I could couple into a SMF in the detection part at the right wavelength, because the beam path of the $785\,\text{nm}$ backreflection is sufficiently different to not provide a good incoupling efficiency at $1310\,\text{nm}$, let alone at $1550\,\text{nm}$.
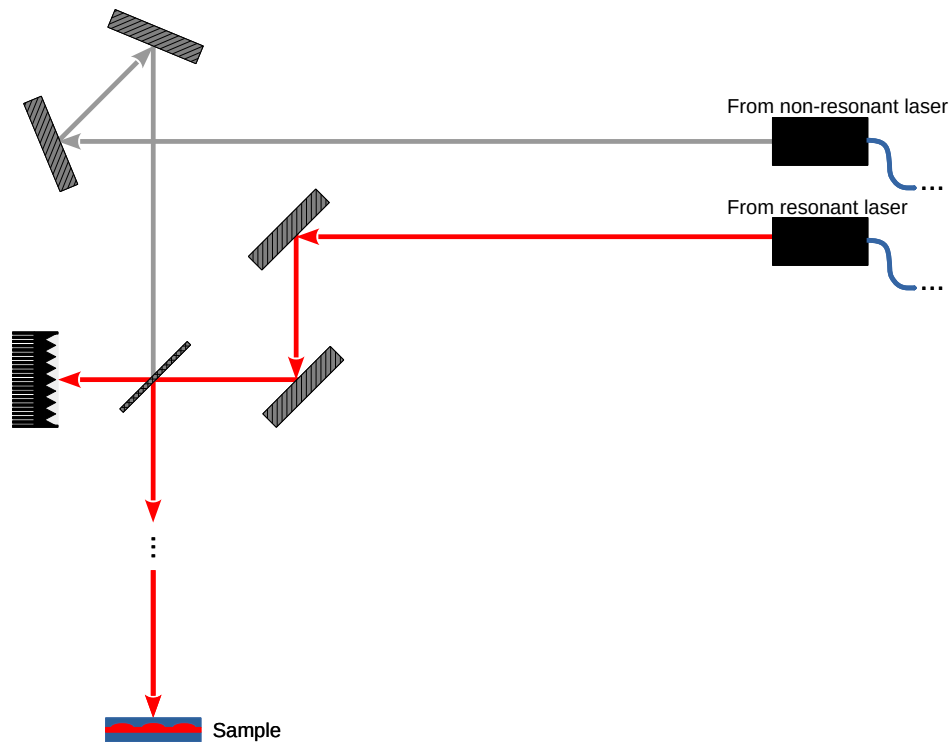
Figure 3.5: The resonant excitation path made of the fibre coupler to the $1310\,\mathrm{nm}$ or $1550\,\mathrm{nm}$ excitation Continuously Tunable Laser (CTL) and two mirrors added to the setup.

Imaging Subsystem

The beam traverses the area of the imaging system in order to reach the two mirrors which guide it down to the cryostat. The imaging subsystem can be engaged by dropping in a $45°$ rotated $55\,\%$ transmission pellicle from *Thorlabs* [48] onto its magnetic mount, s.t. light to illuminate the sample can go down to the cryostat (see Figure 3.6) and backreflections from the sample can go into the imaging system via the same path (see Figure 3.7).

Illumination Subsystem   To illuminate the sample I used a fibre coupled light source. For different use cases I had three different sources available, $\mathrm{viz.}$:

- A $1050\,\text{nm}$ imaging Light Emitting Diode (LED) *Thorlabs M1050F3*. [49].

- A $1450\,\text{nm}$ imaging LED *Thorlabs M1450F1*. [50].

- An *Ocean Insights HL-2000-LL* white light source. [51]

In order to illuminate the whole Field of View (FoV) on the sample given by the objective in the cryostat it is beneficial to collimate the uncollimated light exiting the fibre (lower right in Figure 3.6) to a beam diameter which is bigger than the lens diameter of the objective to ensure full illumination of the lens. In order to do that I chose a lens and positioned it on a cage rod system in front of the fiber, s.t. the beam is collimated. The light is then routed via two mirrors and a fixed $55\,\%$ transmission pellicle [52] to the removable pellicle on the magnetic mount leading to the cryostat. The described illumination path can be seen in red in Figure 3.6.

Micrometer Scale Imaging   The backreflected illumination light is re-entering the imaging subsystem through the removable pellicle again. The light is then routed via the fixed pellicle and two mirrors for alignment onto the sensor of the *Xenics Bobcat 320 GigE* camera [53].

Widefield Microscopy   In the imaging system I mounted another drop-in pellicle which guides the backreflections from the sample down another path with two[3] mirrors in a cage-rod system to the *Princeton Instruments NIRvana 640* camera [54] for widefield microscopy. This can be used to image a big part or even the whole sample at the same time without scanning the position. If the sample is then illuminated with a suitable imaging LED which excites QDs on it (e.g. the *Thorlabs* $1050\,\text{nm}$ LED), it is easy to identify and localise very bright QDs to be measured. This would significantly cut down the time to find a QD on a sample in the future, but it was not implemented due to the time constraints associated with this thesis.

Excitation in the Cryostat

The light enters the cryostat from above, routed from the imaging system's bread-board down, through the window of the outer cryostat shroud (vacuum isolation) and the window of the inner cryostat shroud (heat isolation). In the cryostat the *LT-APO/IR/0.81* apochromatic cryogenic objective by *attocube* [55] is mounted on a piezo z-stage which can move it up and down in order to focus on different points of the sample/sample holder. The samples

---

[3]NB Only one mirror is shown in the schematic as the path is in reality downwards from the bread-board and the camera is mounted underneath it, which is indicated by the dash-dot line perpendicular in the beam path.
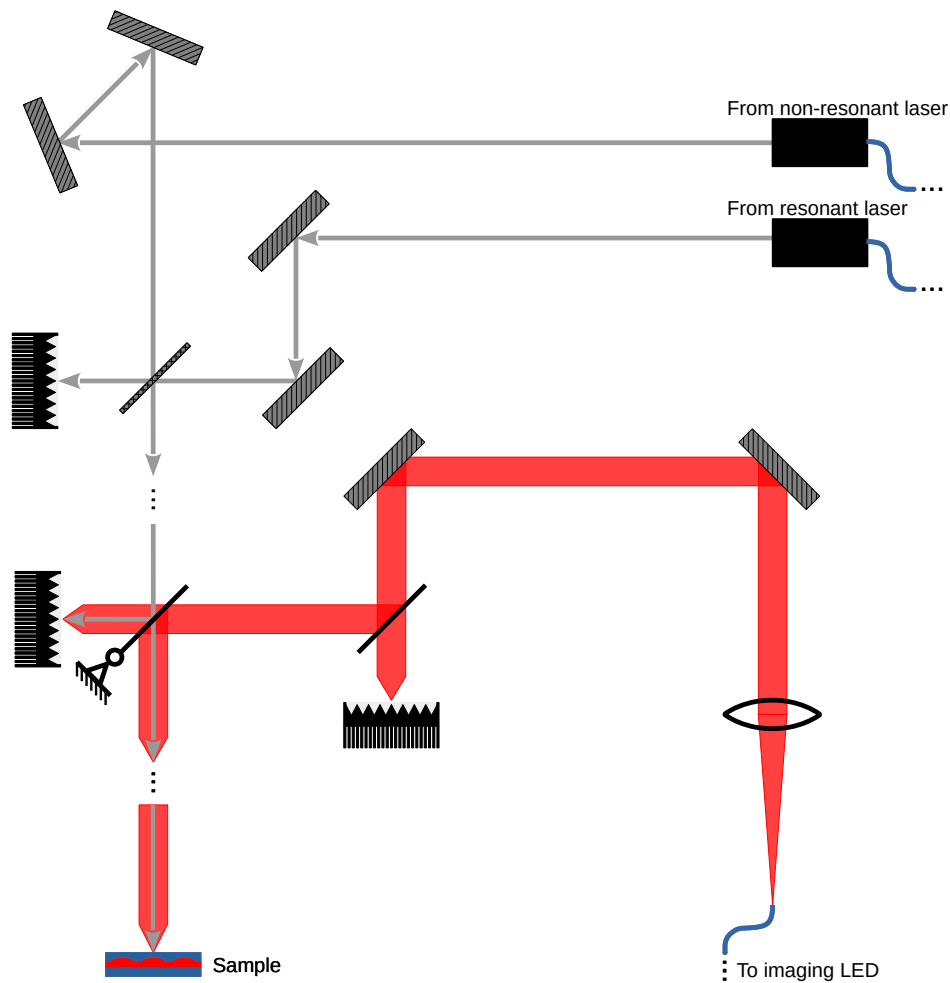
Figure 3.6: The illumination path made of the $1050\,\mathrm{nm}$, $1450\,\mathrm{nm}$ or white light source connected to a bare fibre, a collimation lens, two mirrors, a fixed and a removable pellicle, and suitable beam dumps added to the setup.

are mounted on the sample holder, which is thermally contacting the cold-head of the cryostat to cool the sample. Sample holder can be moved in x- and y-direction to investigate different positions on the sample. The focused incoming light excites the sample (in case of the excitation lasers) or illuminates it (in case of the illumination light sources). The backreflections and emissions from the sample leave through the objective again to be detected by the imaging cameras or the spectrometer.

From non-resonant laser

From resonant laser

Beams/reflections which serve
no purpose after that point are
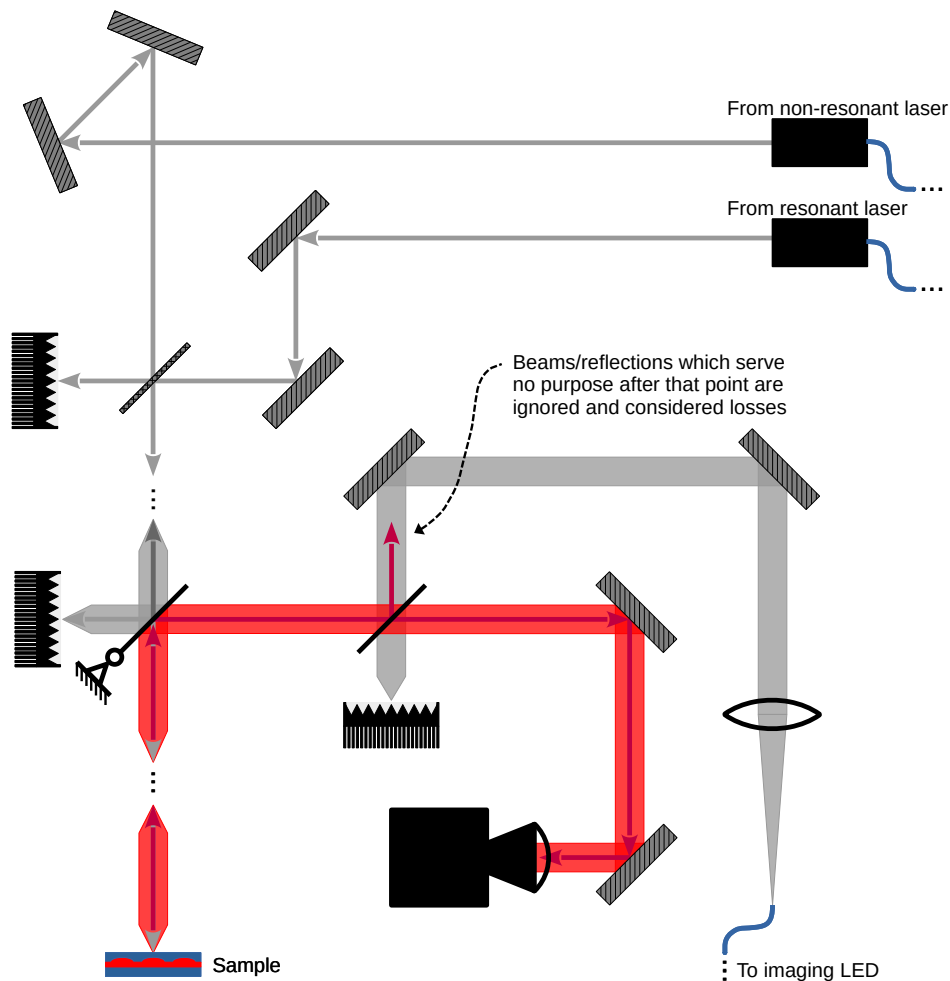ignored and considered losses

Sample

To imaging LED

Figure 3.7: The path for micrometer scale imaging made of two additional mirrors and the
Bobcat camera added to the setup.

Detection Path

The detection path is the last branch of the free-space setup on the main PL bread-board.
It is separated from the other paths via aforementioned *Thorlabs BS066* non-polarising BS
cube with 70% reflectance [47] and collects backreflections and emissions from the sample
(if they are not going down a path in the imaging system already). The backreflections may
be filtered out of the detected signal by choosing the appropriate filtering methods suitable
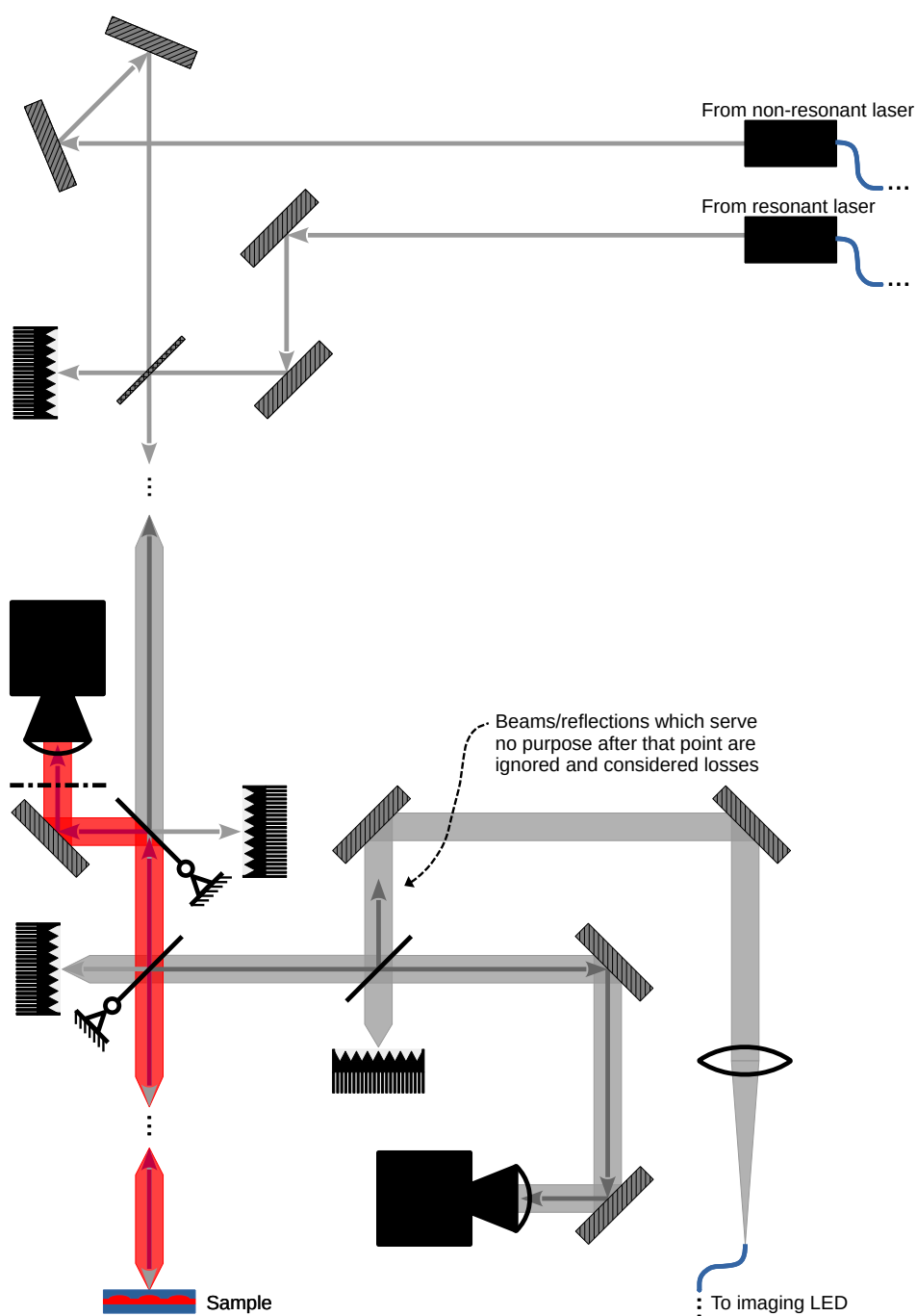for the specific application. This concludes the description of the free-space setup.

Figure 3.8: The path for widefield microscopy made of a removable pellicle to activate the path, two additional mirrors (only one of which is shown in the schematic), and the *NIRvana* camera added to the setup.
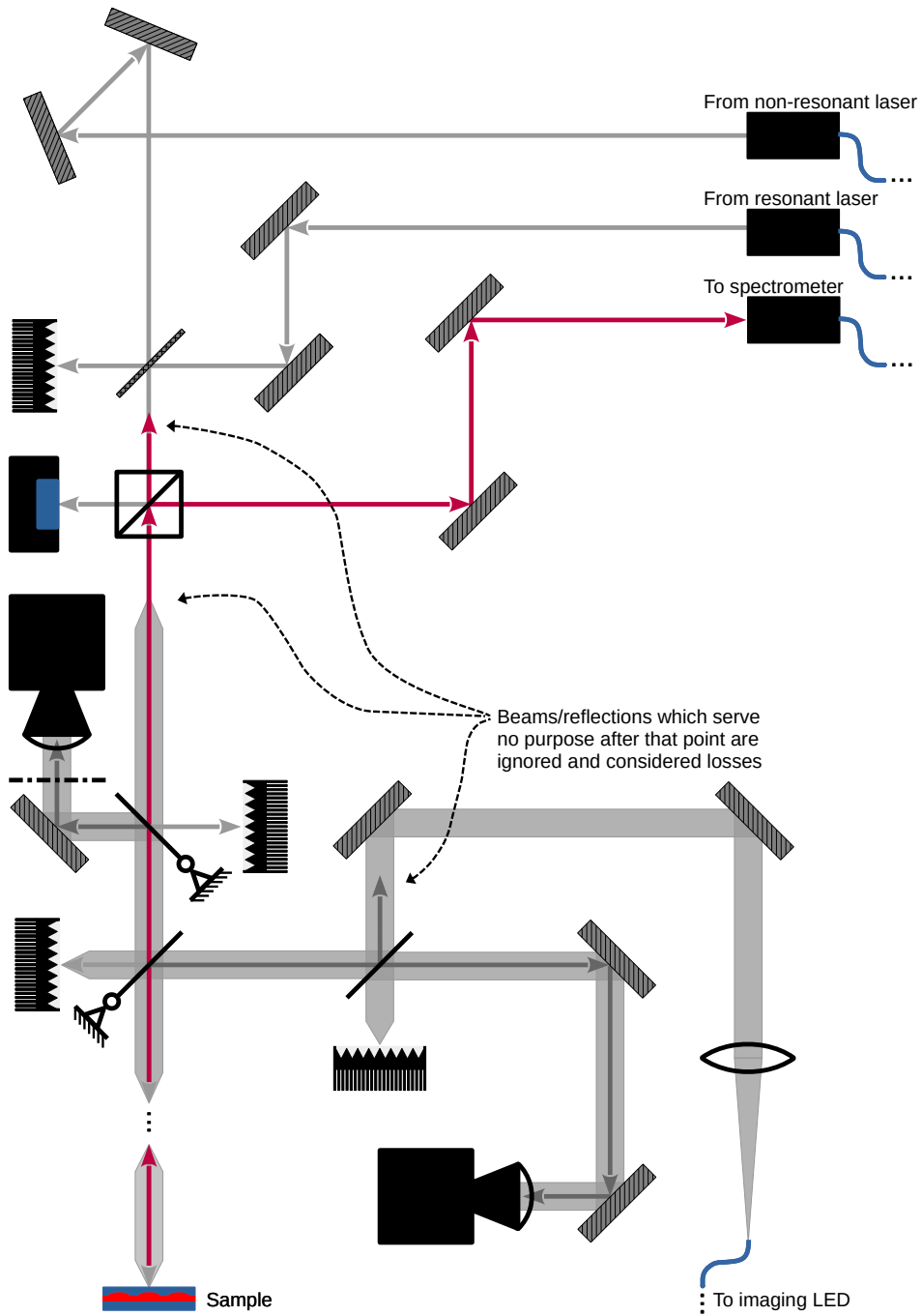
From non-resonant laser

From resonant laser

To spectrometer

Beams/reflections which serve
no purpose after that point are
ignored and considered losses

To imaging LED

Sample

Figure 3.9: The path for the emissions made of a non-polarising BS cube and two mirrors
added to the setup.

3.2 Spectrometer Subsystem

After the emissions from the samples are coupled into an optical fibre they are guided into the spectrometer subsystem, which will be described here.

The *Shamrock 750* spectrometer from *Andor* with $750\,\text{mm}$ has two entrances (labelled *Side* and *Direct*). The entrance to be used can be specified in the spectrometer software. In our setup the *Direct* entrance is dedicated to collection with a Multi-Mode Optical Fibre (MMF), while the *Side* entrance is dedicated to collection with a SMF. Doing so allows to couple in many modes without needing to touch the incoupling for a single one all the time. The light is coupled out with a *Schäfter+Kirchhoff* collimator either with a MMF or a SMF depending on the entrance of the spectrometer. After that the light is routed via one mirror to a lens which focuses the beam on the adjustable slits on the respective entrance of the spectrometer. The slit can be tuned to let in more light at the cost of resolution of the spectrometer, so a compromise between the two has to be found for a specific application. [56]

The spectrometer has two camera exits also labelled *Side* and *Direct*. The used exit can be chosen in the control software. A 1D InGaAs Charge-Coupled Device (CCD) camera array with $1024\,\text{px}$ was mounted onto the *Direct* output. Only this camera is suited for our experiments, because the other camera mounted on the *Side* entrance is a 2D Si-array which cannot detect radiation in the suitable wavelength range. [56]

The spectrometer has a motorised tower with three diffraction gratings, which perform the FT to the spectral domain for the incoming light. They can be moved in a way that the desired spectral part of the light hits the sensor and can be measured. The grating with the lowest spectral resolution of $0{,}35\,\text{nm}$ has $150\,\text{lines}/\text{mm}$, the second grating has $600\,\text{lines}/\text{mm}$ with a higher resolution of $0{,}09\,\text{nm}$ and the third grating has $1200\,\text{lines}/\text{mm}$ and thus the highest resolution of $0{,}04\,\text{nm}$. The third grating was not used in our measurements because it has low efficiency in the O-band and is not suited for the C-band. [56]

4 Data & Analysis

As described in Section 2.4 a first measurement to establish the quantum nature of the emissions from our sample is a PL measurement on single QDs. These µPL measurements were conducted with my setup to inspect single QD emissions. More specifically we conducted µPL measurements with a series of different powers to investigate the power dependency of the emissions. Additionally, we performed polarisation dependent measurements to investigate the polarisation dependence of the integrated intensities of emission lines in order to investigate DOLP and FSS. First we investigated the reflective properties of the DBR on the sample emitting in the C-band to validate the setup. We conducted PL measurements on the sample emitting in the C-band where we were able to identify different excitonic transitions by power dependent measurements. Polarisation resolved measurements allowed the measurement of FSS and identification of biexciton-exciton cascades. Next we investigated the sample emitting in the O-band, where we were able to identify biexciton-exciton cascades through power dependent and polarisation measurements and subsequent calculation of FSS. Furthermore, we show PL spectra which arise from recombinations from discrete p-shell states and analysed their polarisation dependent behaviour. The behaviour of the p-shell states was also compared to the behaviour of the s-shell states. And finally, the improvement of the collection efficiency of photons emitted from the sample emitting in the O-band via SILs was evaluated and an improvement of up to $\sim 146\,\%$ was observed.

4.1 Micro-Photoluminescence on the Sample Emitting in the C-Band

For the measurements on the sample emitting in the C-band we used the laser at $785\,\mathrm{nm}$ for above bandgap excitation and the grating of the spectrometer with $150\,\mathrm{lines/mm}$ which has a Dispersion Window (DW) of about $225\,\mathrm{nm}$. A typical spectrum showing sharp peaks from recombinations of a single QD at excitation power $0{,}41\,\mathrm{\mu W}$ can be seen in Figure 4.1. The captured data was baseline corrected by subtracting the average of multiple spectra of just the noise background of the spectrometer's InGaAs CCD sensor. In the graph the emission line at higher wavelength was identified as the exciton and the bright line next to it as the

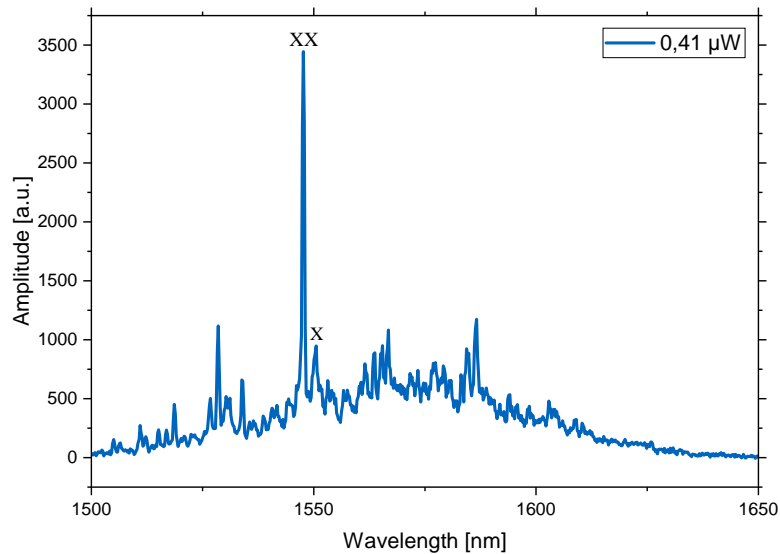biexciton.[1] They were identified with the procedure described in the following sections.

Figure 4.1: A typical spectrum for above bandgap excitation at $0{,}41\,\mu W$ excitation power. Exciton and corresponding biexciton of a single QD are marked.

4.1.1 Distributed Bragg Reflector on the Sample Emitting in the C-Band

The first step for validating the setup is to be sure that we focus on the sample and show that we can actually measure some data which is known a priori. Thus, we engaged the imaging system via the drop-in pellicle and moved the sample in x- and y-direction with the piezo actuators. We searched for an edge visible with the *Bobcat* camera – which is hopefully the edge of the sample. Then we focused on the surface near the edge with the z-direction piezo. To confirm that we are indeed on the sample this surface should exhibit the reflective properties created by the DBR underneath. To do this we used the *HL-2000-LL* white light as an illumination source whose reflection will go down the detection path (see Figure 3.9), where it was coupled into a MMF and sent to the spectrometer. We had to stitch together multiple captured spectra from the spectrometer to investigate the spectrum of reflected light shown in Figure 4.2. This was caused by the usage of the lowest resolution grating of the spectrometer which has $150\,\text{lines/mm}$ and a DW of around $225\,\text{nm}$. That is, the InGaAs CCD sensor of the spectrometer captures a spectral range of $\sim 225\,\text{nm}$ at a time. When we compared the measured reflected light given in Figure 4.2 to the reflectivity of a sample grown with the same process by Zeuner in [14] we could see clearly the dip in reflectivity around

---

[1]Whether the energy of the biexciton or the exciton is higher may also depend on QD size.

1450 nm in both of them. That shows firstly, that the setup works as expected, secondly, that we are indeed focusing on the sample, and thirdly, that the DBR also does its job.
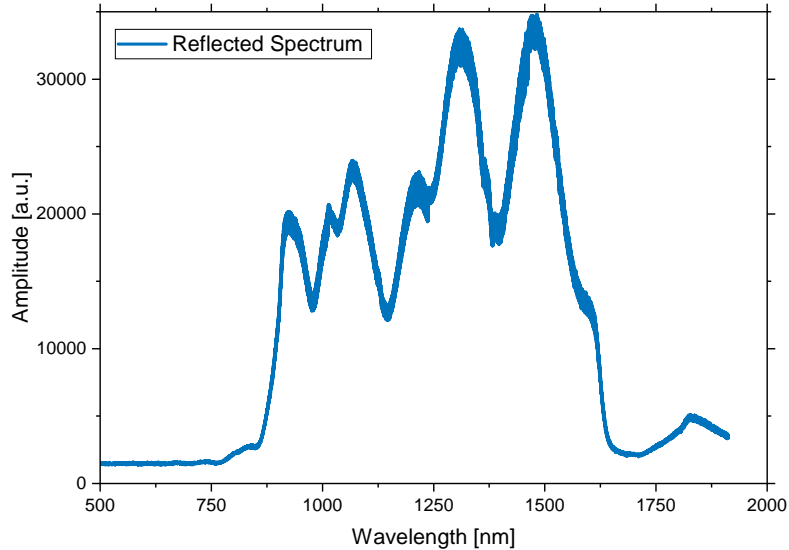

Figure 4.2: Spectrum of the white light source reflected from the sample emitting in the C-band.

4.1.2 Power Dependent Measurements on the Sample Emitting in the C-Band

To conduct a power series the excitation was carried out with a laser at 785 nm at a fixed power. Then we step through the FAB attenuation values with constant steps (see Figure 3.1 for the output powers of the FAB). For every output power a spectrum is captured for a given integration time of the sensor. The power value which is measured at the power meter mounted on the BS cube (can be seen in Fig. 3.3) is recorded alongside the corresponding attenuation factor and spectrum. The power values are thus roughly 70 % of the power sent into the system, while 30 % are sent further. How much power is reaching the sample is not known perfectly, but the losses in the setup can be assumed to be constant. This means as long as we consistently measure the power at the same position it is directly proportional to the power reaching the sample. After one measurement we repeat this for the next power value. The granularity (and even a different function of power, see Section 3.1.1) of the measurement can be changed in software. Like this we are able to capture data showing power dependent behaviour of a QD on the sample.

The typical emissions from the sample emitting in the C-band behave as is shown in Figure 4.3. For a small power at some point the emissions from the QDs start and spectral peaks
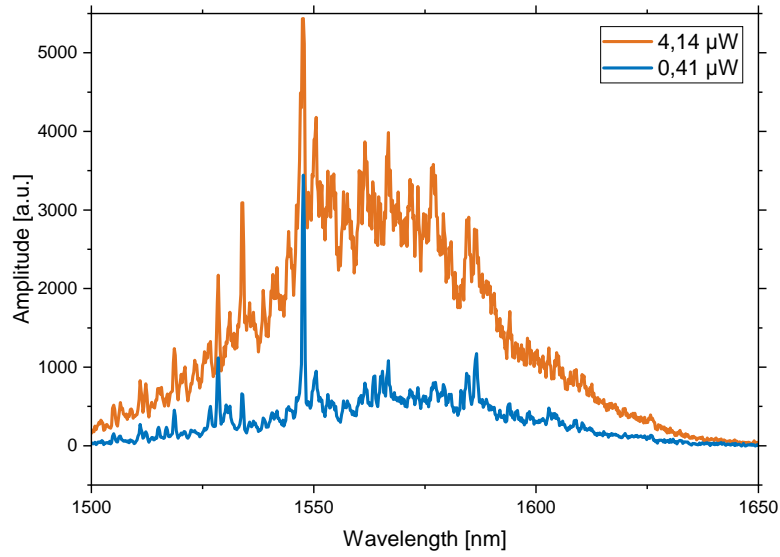
Figure 4.3: Spectra for $0{,}41\,\mu\text{W}$ and $4{,}14\,\mu\text{W}$ excitation power.

appear, e.g. the blue spectrum for $0{,}41\,\mu\text{W}$ in Fig. 4.3. For progressively higher power the peaks are brighter and new ones may appear for different transitions. Some transitions will saturate at a certain power as they are driven as fast as they decay, which is a limiting factor on the transitions' brightness. This behaviour is clearly visible for the orange spectrum for $4{,}14\,\mu\text{W}$ in Fig. 4.3. But additionally in this spectrum it is also visible that there is not only an increase in brightness and number of the peaks, also the background is increasing for higher power in an almost Gauß-like fashion. This behaviour was present in almost all measurements on this sample. It is probably the broadband emission from the MBL, which also gets excited by the above bandgap excitation laser.

Different states of a QD can not only be characterised w.r.t. their energy levels but also in terms of its charging behaviour: we can look at the transitions regarding the number of charge carriers – and in turn number of excitonic quasi-particles – which are involved. If a QD is charged – i.e. filled with charge carriers – with a constant rate resulting in the mean exciton number $\bar{n}$, the probability distribution for finding n excitons in the QD is a Poissonian (remember Equation 2.3):

$$\mathcal{P}(n) = \frac{\bar{n}^n}{n!} e^{-\bar{n}}. \tag{4.1}$$

This assumes aforementioned constant charging rate and that carriers are filled into the QD independently and finally, that excitons also recombine independently. It seems reasonable to assume a constant charging rate for a constant power output of the excitation laser. Varying

the laser power can be used to change $\bar{n}$. And for low powers ($\hat{=}$ $\bar{n} \longrightarrow 0$):

$$\mathcal{P}(n) \approx \frac{\bar{n}^n}{n!}. \tag{4.2}$$

That means that for X we have approximately $\mathcal{P}(1) \propto \bar{n}$ and analogously for XX: $\mathcal{P}(2) \propto \bar{n}^2$. If we now logarithmically plot the power dependency of peaks under consideration, the slopes show the charging behaviour of the QD. Thus, it should be possible to fit a linear function to the data in the low power regions (as not to violate the assumption making our approximation valid). This linear function should then have a slope of around 1 for X and 2 for XX. [23, pp.23 et seq.]

Nevertheless, it also has to be kept in mind, that the charging and recombination behaviour of a QD may not adhere completely to the assumptions we made. For example, interdependence of different excitonic quasi-particles or saturation effects may and higher power effects will give rise to deviations from this approximation, but this is to be expected from a simple approximation for a rather complex process. [57]

The results of the power series measurements and according analysis on the sample emitting in the C-band can be exemplified by Figure 4.4. The peaks were extracted from the spectra for every power and then fit with a Lorentzian. The Lorentzian has to be integrated over amplitude, because of the uncertainty principles at play (cf. Section 2.2.3). The integrated amplitude values are then plotted as a function of power for the different peaks and linearly fitted to extract the power law described above. This can be seen for an exciton and biexciton in Fig. 4.4.

Peaks which showed the desired slopes of ~ 1 for X and ~ 2 for XX in low power regions could thus be preliminarily identified as candidates for excitonic and biexcitonic transitions. But to increase the certainty that one is currently looking at a peak from an exciton and biexciton further analysis has to be done.

4.1.3 Polarisation Dependent Measurements on the Sample Emitting in the C-Band

After the power series we can be reasonably sure which peaks from a QD's emission are biexcitonic and which are excitonic emissions, but to further confirm our hypothesis we will investigate the polarisation dependence of the emission. To investigate the polarisation dependent intensity of the emissions we mount a $\frac{\lambda}{2}$-plate[2] onto a *CONEX AG-PR100P* mo-

---

[2]This will rotate the linearly polarised light by 2θ, where θ is the angle between the polarisation direction and the so-called *fast axis* of the $\lambda/2$-plate.
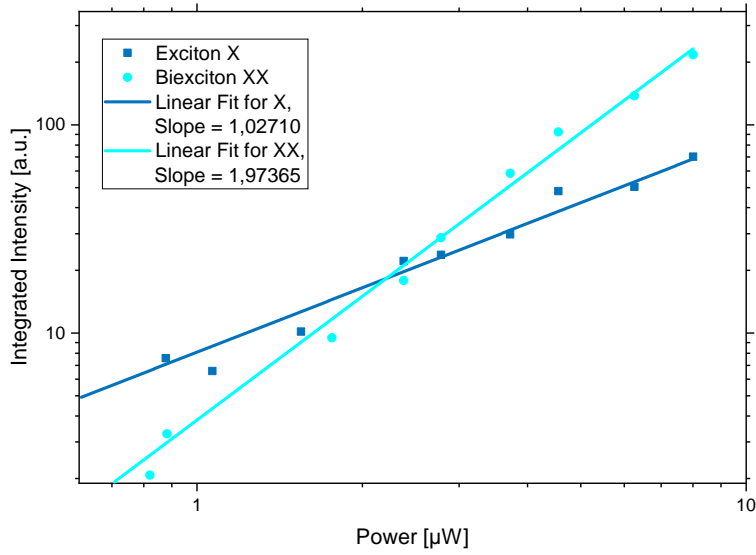
Figure 4.4: Linear fit of integrated intensities of exciton and biexciton peaks to show their power dependence.

torised rotation stage from *Newport* where optics may be mounted and rotated automatically and precisely. Afterwards we mount a fixed linear polariser which performs a projective measurement (see Section 1.3.1) of the light onto its axis. We also filter out the non-resonant excitation laser beam at $785\,\text{nm}$ with a long-pass filter with cutoff wavelength of $850\,\text{nm}$. This way we are able to analyse the different polarisations with the spectrometer. We rotate the motorised stage with $4°$ steps and take a spectrum with an appropriate integration time after each step. This is how we generated the data sets for the following analyses.

Fine Structure Splitting on the Sample Emitting in the C-Band

Due to the difference in lattice constant for different spatial directions the QDs will probably be also asymmetric. This leads to anisotropic confinement and thus a FSS. If the FSS is too small for the spectrometers resolution it cannot be directly observed from a single non-polarisation-resolved spectrum. However, it is possible to suppress one of the polarisation components with the setup described above and then the peaks can be fit. Via this method the FSS should become apparent in our polarisation dependent measurements because of the spectral oscillation (i.e. energy shift) for the different polarisations emitted by the biexciton-exciton cascade as described in Section 2.2.2. [14, p.49]

For the sample emitting in the C-band we can see such spectral oscillations in Figure 4.5. For

each spectrum the peaks were fit with a Lorentzian. The figure shows that the maxima of the Lorentzian fit exciton and biexciton peaks oscillate spectrally. This oscillation can be fit with a sinusoidal function and the amplitude of the fit corresponds then to the FSS. In this example we have an oscillation of in total $0{,}039\,59\,\text{nm}$ around the central wavelength $1528{,}45\,\text{nm}$ for the biexciton – which corresponds to an energy[3] of $E_{V_{\text{XX}}} - E_{H_{\text{XX}}} \approx 21{,}011\,\mu\text{eV}$[4] – and $0{,}040\,01\,\text{nm}$ around $1533{,}93\,\text{nm}$ ($\approx 21{,}083\,\mu\text{eV}$). They are very close, which is a good indication that those peaks are in fact emissions from the same QD. But as speculated in Section 2.2.2 they are not completely identical, probably due to some noise, numerical inaccuracies in the fitting, and so on. Thus, we use Equation 2.22 to calculate the average of both which is $21{,}047\,\mu\text{eV}$. This aligns really well with the FSSs which are reported in [14]. Also in [58] InAs QDs on an InGaAs MBL emitting in the C-band are studied and they report a mean FSS of $23{,}4\,\mu\text{eV}$, which is in the same range. It is important to note that the horizontal or vertical directions of the polarisation can be chosen arbitrarily here, because changing it would be just a *Galilean transformation* (i.e. change of reference frame). Thus, the sign of the FSS coming from our calculation would be meaningless. It is just the case that we have to be consistent with the definition of horizontal and vertical within the measurement of a single QD. Thus, we can assume without loss of generality that the first minimum (maximum) of the sine fit corresponds to horizontal (vertical) polarisation. Therefore, it is valid to calculate the FSS like this. This is also the reason why excitonic and biexcitonic peaks coming from the same QD have to oscillate $90°$ out of phase, which helps us identifying peaks/reassuring us in our decision.

Degree of Linear Polarisation on the Sample Emitting in the C-Band

As mentioned in Section 2.2.4 the DOLP is a measure to characterise how much of an emission is polarised in what way. In order to calculate the DOLP we recall Equation 2.23: we need to look at the polarisation dependent intensity extrema of the peaks. In Figure 4.6 we can see the intensity fluctuations of an exciton and corresponding biexciton (in this case emissions at $1568{,}1\,\text{nm}$ and at $1568{,}9\,\text{nm}$) depicted as a polar plot. Remember that the biexciton-exciton pair oscillates $90°$ out of phase spectrally because of the FSS. The intensity fluctuations on the other hand are in phase as can be clearly seen from Fig. 4.6. This suggests a global anisotropy regarding the polarisation of the emission affecting both transitions in the same way. To quantify the DOLP we fit the data with a sinusoidal function to get the maximal and minimal intensities and then calculate the DOLP value according to Equation 2.23. This way we get $DOLP_\text{X} = 7{,}896\,\%$ and $DOLP_\text{XX} = 7{,}928\,\%$ for this particular QD. Both values being similar could be another indicator that both peaks are indeed from the same QD. On the other hand the DOLP data from this sample seems not to be really reliable,

---

[3]$\lambda \propto \frac{1}{E}$ through the *Planck-Einstein relation* $E = \frac{hc}{\lambda}$.
[4]Although not an *SI*-unit it is customary to use *electronvolts* in this context: $1\,\text{eV} := 1{,}602\,176\,634 \cdot 10^{-19}\,\text{J}$.
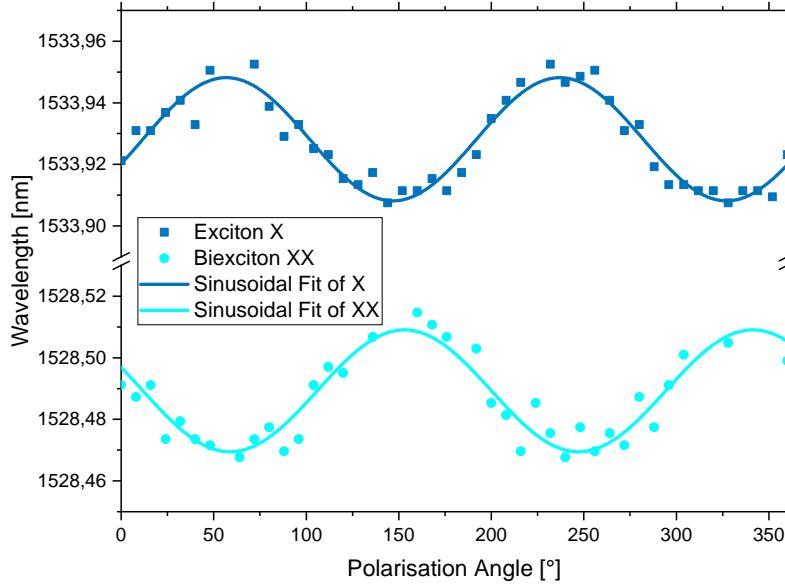
Figure 4.5: Spectral oscillation of exciton and biexciton peaks in a polarisation dependent measurement taken at power of $\sim 2{,}19\,\mu\text{W}$.

because this relationship was not clear for most of the QDs investigated and also the lowest value calculated was $DOLP = 5{,}144\,\%$ and the highest $DOLP = 18{,}425\,\%$. This suggests significant variance even within the sample, while the results from [27] show such differences in DOLP for different samples with different In content in the MBL. Extrapolating from the results in [27] suggests that for higher In content in the MBL (and in turn higher emission wavelength) the DOLP should increase. We could not really see this on the sample emitting in the C-band as it has a composition of $\text{In}_{0{,}4}\text{Ga}_{0{,}6}\text{As}$ on the top of the MBL, which should yield even more than the $16{,}5\,\%$ DOLP for $\text{In}_{0{,}29}\text{Ga}_{0{,}71}\text{As}$ in [27], but the values ranged from $5{,}144\,\%$ to $18{,}425\,\%$ as mentioned before. Due to the scope of this thesis and the focus on the sample emitting in the O-band, a statistical analysis of many DOLP values on the sample emitting in the C-band was not carried out. As such the conclusions drawn from this limited analysis have to be considered inconclusive.

4.2 Micro-Photoluminescence on the Sample Emitting in the O-Band

Power dependent and polarisation dependent measurements are also reported for QDs on the sample emitting in the O-band. Furthermore, we showed an increase in collection
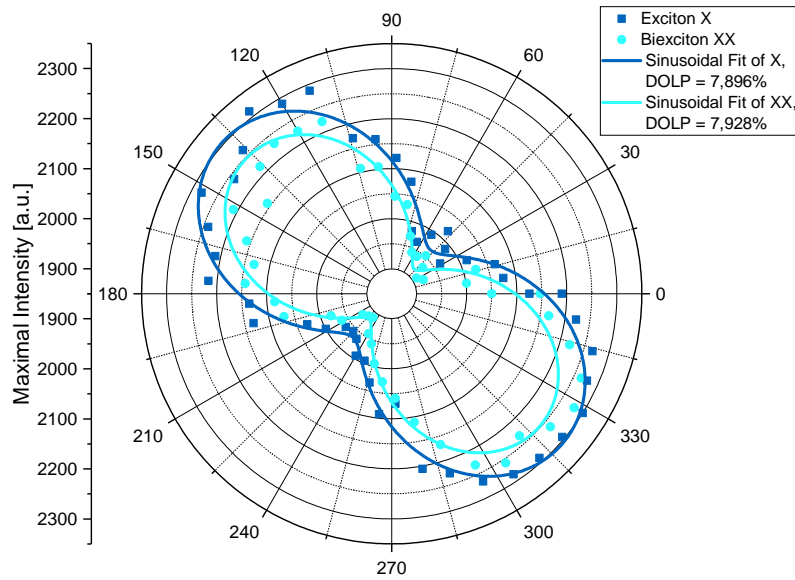
Figure 4.6: Polar plot of exciton and biexciton intensity dependent on polarisation.

efficiency from the sample emitting in the O-band with the use of SILs. We used the grating with $600\,\text{lines/mm}$ and DW of around $50\,\text{nm}$ for this wavelength range, which increased the resolution of the measurements considerably, albeit at the cost of some counts, which made it necessary to sometimes increase the integration time of the spectrometer's CCD prolonging the time for each measurement.

Before being able to use our setup for the new sample though it had to be realigned for detection around $1310\,\text{nm}$, meaning that I used the *CTL 1320* at $1310\,\text{nm}$ in the resonant excitation path (see Fig. 3.5) and overlapped its laser spot on the same spot on the sample as the excitation laser – which is the same $785\,\text{nm}$ laser as before. The CTL's backreflection then serves as a mimicked emission used to couple into the fibre in the detection path (Fig. 3.9). This was necessary because the beam path changes significantly for the new wavelength range.

4.2.1 Power Dependent Measurements on the Sample Emitting in the O-Band

The power series was performed in the same way as described in Section 4.1.2. In contrast to the results from the sample emitting in the C-band we encountered a very interesting behaviour. As Figure 4.7 illustrates, the spectra obtained at different powers of $28{,}20\,\mu\text{W}$ and $2{,}73\,\mu\text{W}$ seemed similar to the spectra gathered from the sample emitting in the C-band.

But with increasing power not only the background increased[5], the visible emissions showed saturating behaviour, and new emission lines appear, additionally also the emission lines at higher wavelengths disappear with increasing power and others appear at lower wavelengths. This is shown exemplary in Fig. 4.7: at an excitation power value of 2,73 µW the most visible peaks are around 1275 nm. But those peaks vanish, while peaks of a similar number and intensity appear in a lower wavelength (and thus higher energy) region around 1250 nm. Similar behaviour could be observed for almost all QD emissions on this sample around their respective emission wavelengths. This lead us to believe that we observe emissions from the s-shell of the QDs for lower powers, while we excite p-shell states for higher powers. Regarding excitation powers it has to be mentioned that lower counts and higher excitation powers for similar emission characteristics are to be expected from the sample emitting in the O-band compared to the sample emitting in the C-band because of its unoptimised nature and lack of DBR. This is exactly what we see in Fig. 4.7 compared to Fig. 4.3: less counts for higher excitation powers.
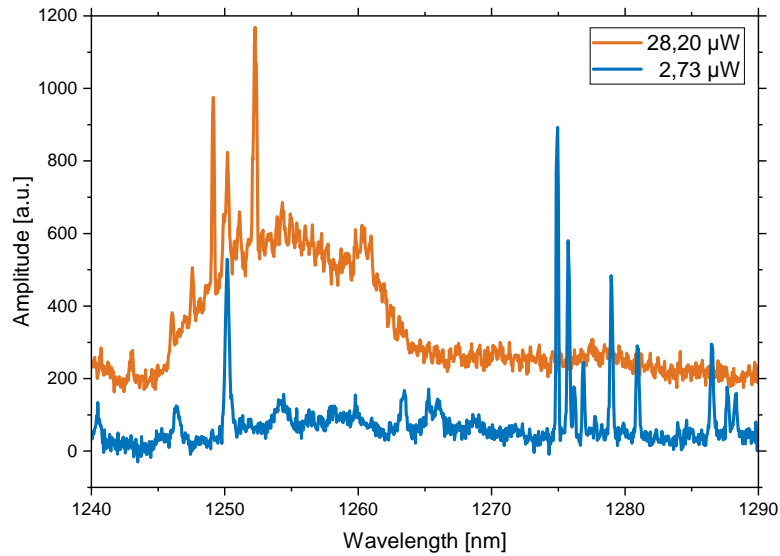

Figure 4.7: Spectra for 2,73 µW and 28,20 µW excitation power.

Before investigating this any further in Section 4.2.3 we have a look at the transitions driven at low powers to compare to the sample emitting in the C-band. As described in Section 4.1.2 the approximation of the power dependency from Equation 4.2 is only valid for low powers. Thus, we investigated QDs accordingly. We will discuss our data exemplary on a QD which has peaks XX, X, and $X^{\pm}$ shown in Fig. 4.8. In the figure a partial spectrum for excitation power of 1,72 µW is shown. In the following we will look at biexciton XX at wavelength 1279,60 nm, exciton X at 1278,97 nm, and trion $X^{\pm}$ at 1277,93 nm as an illustration

---

[5]Because of the MBL emission from above bandgap excitation.

of the behaviour of most emissions we encountered. $X^\pm$ is found at lower wavelength w.r.t. X (i.e. $\sim 0{,}789$ meV higher energy in this case), which could indicate a positive trion, because according to [23] negative trions were measured 2 meV to 9 meV lower in energy for InAs QDs on GaAs and conversely, the same source also mentions that positive trions in InAs QDs on GaAs were generally 1 meV to 14 meV higher in energy than excitons. But because there were also positive trions with energies lower by 1 meV than the exciton [23, pp.19-21] and we used an MBL in addition to normal GaAs substrate this may change the energy difference between X and $X^\pm$. Thus, it is not really clear if we observe a negative or positive trion, while a positive one seems more likely.
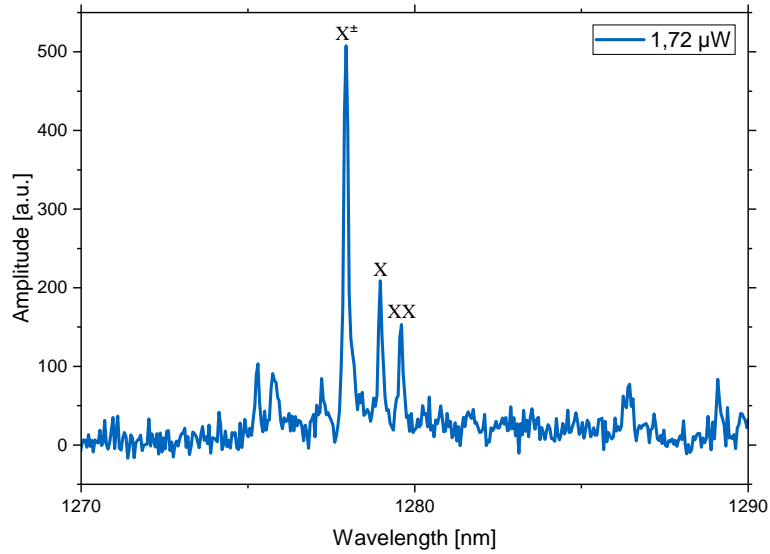

Figure 4.8: A spectrum for above bandgap excitation with excitation power $1{,}72\,\mu$W. Biexciton XX, exciton X, and trion $X^\pm$ under investigation are marked.

We can again assume that Equation 4.2 holds for low powers and thus fit the data points linearly in the $\log_{10}$-$\log_{10}$-scale plot as excitonic transitions should scale according to the power law $\mathcal{P}(1) \propto \bar{n}$ and biexcitonic transitions according to $\mathcal{P}(2) \propto \bar{n}^2$. Trion states can be seen as intermediates between excitons and biexcitons as they have one more bound charge carrier than an exciton and one less than a biexciton (see Fig. 2.3). Thus, it is reasonable to assume that this can be approximated as a mean exciton number n involved in the transition which is higher than 1 for the exciton, but lower than 2 for the biexciton. That means if we set e.g. $n = 1{,}5$ we get $\mathcal{P}(1{,}5) \propto \bar{n}^{1,5}$, corresponding to a slope of $1{,}5$ for a linear fit in $\log_{10}$-$\log_{10}$-scale.

If we now have a look at the linear fits of XX, X, and $X^\pm$ shown in Figure 4.9a we see the following: XX has a slope of around 2 which would indicate a biexcitonic power dependency, while X has a slope of around 1 indicating an excitonic emission. And indeed, also $X^\pm$ has

a slope of ca. 1,5 which we would expect for a trion. It is important to note that we see a nonlinear behaviour for the slope of $X^\pm$ for the higher powers in the diagram. The curve starts to flatten, which corresponds to a saturation of given transition. Thus, the linear fit has to be done up to the data points which are still behaving linearly with power and not any further as our approximation starts to break down. Additionally the data becomes relatively noisy for even lower powers, which makes it necessary to account for outliers and impedes easy fitting of the data. It would be ideal to have a more stable laser and a more stable way of attenuating the power in the future. In addition, it would be helpful to gather more data in those regions with higher integration times to achieve higher Signal-to-Noise Ratios (SNRs) to facilitate easier fitting and more confidence in the data. Nevertheless, it is a good starting point for further investigation.

If we plot the data in linear scale and fit it with Poissonians directly as seen in Figure 4.9b with exponent n equal to 1, 1,5, and 2 for X, $X^\pm$, and XX respectively we can see that the linear slope approximation for lower powers is indeed justified, even though the Poissonian fit also cannot completely account for saturating behaviour observed for higher powers.
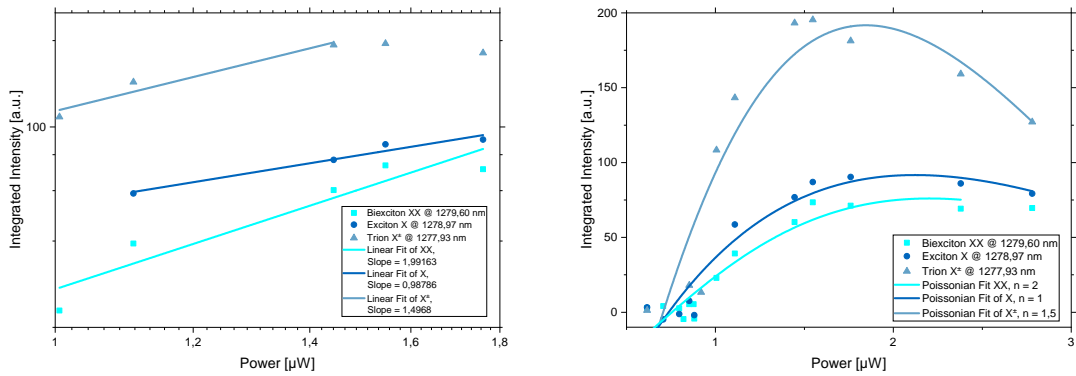
(a) Linear fit of integrated intensities of biexciton XX, exciton X, and trion $X^\pm$ to show their power dependence.

(b) Poissonian fit of integrated intensities of biexciton XX, exciton X, and trion $X^\pm$ to show their power dependence.

Figure 4.9: Comparison of fits of integrated intensities of biexciton XX, exciton X, and trion $X^\pm$ to show their power dependence.

4.2.2 Polarisation Dependent Measurements on the Sample Emitting in the O-Band

The method of gathering data for the polarisation dependent measurements on the sample emitting in the O-band is the same as described in Section 4.1.3.

Fine Structure Splitting on the Sample Emitting in the O-Band

We now look at the polarisation dependent behaviour of XX, X, and $X^{\pm}$ at excitation power of $\sim 1{,}54\,\mu W$. The results of the analysis can be seen in Figure 4.10. We see strong oscillations with $\sim 90°$ phase shift for XX and X with very similar amplitudes. This confirms our hypothesis that XX is indeed a biexciton and X an exciton and both are from the same QD. Furthermore, $X^{\pm}$ is not oscillating at all, which also confirms the line of reasoning regarding its trionic nature. This is supported by the fact that a trionic state is a TLS which has no FSS (see Section 2.2.2).

Regarding the value of the FSS we now describe how the FSS was calculated: the amplitude of the spectral oscillation of XX is determined by the fitting parameter A of the nonlinear sinusoidal fit $y = y_0 + A\sin(\pi(x - x_c)/\omega)$. The parameters were calculated numerically by the *Levenberg-Marquardt* iteration algorithm, resulting in $A = 0{,}029\,00\,nm$. The spectral shift from XX_V to XX_H is $2A = 0{,}058\,00\,nm \,\hat{\approx}\, 43{,}918\,\mu eV$. Analogously for X the spectral shift from X_V to X_H is $2A = 0{,}067\,84\,nm \,\hat{\approx}\, 51{,}420\,\mu eV$. According to Equation 2.22 this results in a FSS given by:

$$FSS = \frac{51{,}420\,\mu eV + 43{,}918\,\mu eV}{2} = 47{,}669\,\mu eV. \tag{4.3}$$

This is around twice what we observed from the sample emitting in the C-band, but this does not necessarily mean that this can be generalised to the whole sample. For example, we also observed FSS of $\sim 21{,}034\,\mu eV$ for other dots albeit with not as clear power dependency (slopes of $1{,}623\,14$ for the biexciton and $0{,}939\,29$ for the exciton). This FSS would be more in line with the other sample. To determine the statistical distribution of FSS values it would be necessary to perform statistical analysis of emissions from many more different QDs, which is out of the scope of this work. The growth parameters for the sample emitting in the O-band are also not yet tuned to minimise FSS for entanglement generation.

Degree of Linear Polarisation on the Sample Emitting in the O-Band

The DOLP was measured and calculated the same way as for the sample emitting in the C-band. In Figure 4.11 we have the polar plot of the polarisation dependent intensity fluctuations of an exciton and biexciton pair (at $1259{,}39\,nm$ and $1258{,}51\,nm$). The calculated DOLP values – calculated via Equation 2.23 – are $DOLP_X = 26{,}158\,\%$ and $DOLP_{XX} = 27{,}999\,\%$ in this case. Again we have in-phase oscillations of intensity and DOLP of the same order of magnitude[6] suggesting emissions from the same QD.

---

[6]Remember, not absolute brightness of peaks is important for DOLP, even though they are very similar in this case. Brightness is also dependent on focus settings, different dispersion for different wavelengths, etc.
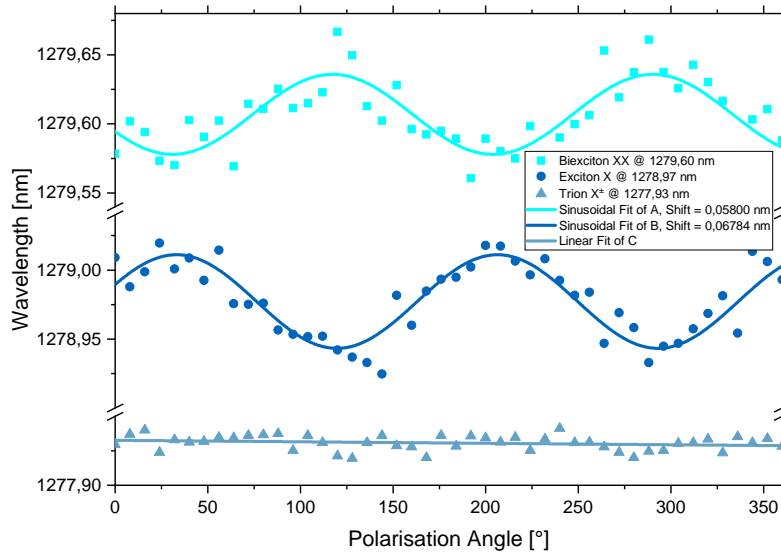
Figure 4.10: Spectral oscillation of the exciton and biexciton peaks and no oscillation of the trion peak in a polarisation dependent measurement taken at power of $\sim 1{,}75\,\mu W$.
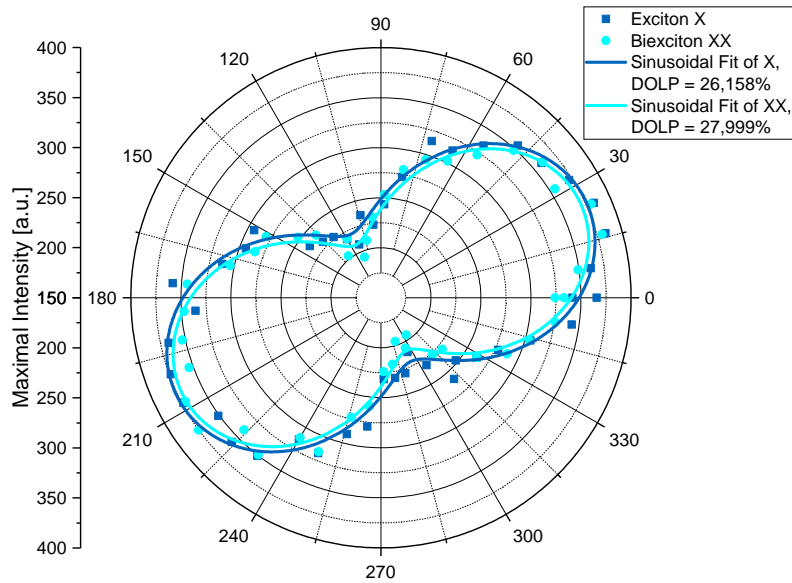

Figure 4.11: Polar plot of exciton and biexciton intensity dependent on polarisation.

The statistics on the DOLP of 19 different emissions[7] yield a mean DOLP of 24,839 % with

---

[7]The number of samples is already corrected for outliers.

standard deviation $5{,}62\%$. Without outliers the minimum and maximum values I calculated were $15{,}555\%$ and $34{,}985\%$, respectively. This is still a relatively large range but most values were clearly around the mean as the variance was relatively low. Again, extrapolation from [27] suggests that for higher In content in the MBL the DOLP should increase. Contrary to the sample emitting in the C-band ($In_{0,4}Ga_{0,6}As$ on top of the MBL), the mean DOLP from the sample emitting in the O-band clearly surpasses $16{,}5\%$ DOLP measured for $In_{0,29}Ga_{0,71}As$ on top of the MBL. [27] This confirms our expectations regarding the effects of the MBL.

We have now analysed the data for the generally expected behaviour from this sample, but as alluded to before we also encountered interesting behaviour in the power series measurements. Thus, we will turn towards the description of those s- and p-shell effects on this sample now, which may yield a promising starting point to explore p-shell excitation schemes for O-band QDs.

4.2.3 s-Shell and p-Shell Energy States on the Sample Emitting the O-Band

We discovered interesting effects on this novel kind of sample emitting in the O-band concerning the s- and p-shell nature of the energy structure of QDs. Thus, we will have a more detailed analysis of the captured data in this section.

Power Dependence of Excitonic Transitions from s-Shell and p-Shell Energy States

The power map in Figure 4.12 shows an example of a QD emitting around $1265\,\text{nm}$. It clearly shows the described behaviour for different powers. For low power we see at least four clear peaks in the region from $1274\,\text{nm}$ to $1280\,\text{nm}$ which exhibit their maximum brightness around $3{,}45\,\mu\text{W}$ of excitation power. Those are labelled as candidates A, B, C, and D. They vanish fast for higher power excitation and also vanish (almost) completely. In their stead four similarly structured peaks E, F, G, and H appear in the region from $1249\,\text{nm}$ to $1253\,\text{nm}$, albeit on a rising background brightness level (around 600 counts; shown in turquoise) and even new emerging peaks for very high powers. Those peaks never completely vanish again but settle at some saturation less than the maximal brightness.

Similar structure for s- and p-shell means in this case a similar brightness distribution and power distribution. To illustrate, the outermost of each quadruplet are the brightest peaks, $viz.$ A and D for the s-shell and E and H for the p-shell. Those are also the first peaks to appear from lower to higher power. The leftmost peaks (A and E) are also the first to vanish (or settle at some saturation level for E). On the other hand the rightmost peaks (D and H) stay bright the longest and the second from the right peaks C and G are starting "latest"

(i.e. for highest power). The second from the left peaks B and F behave similar to the leftmost peaks but a bit dimmer and starting for slightly higher power. This leads to the hypothesis that those peaks are closely related in the pairs $\{(A,E),(B,F),(C,G),(D,H)\}$.
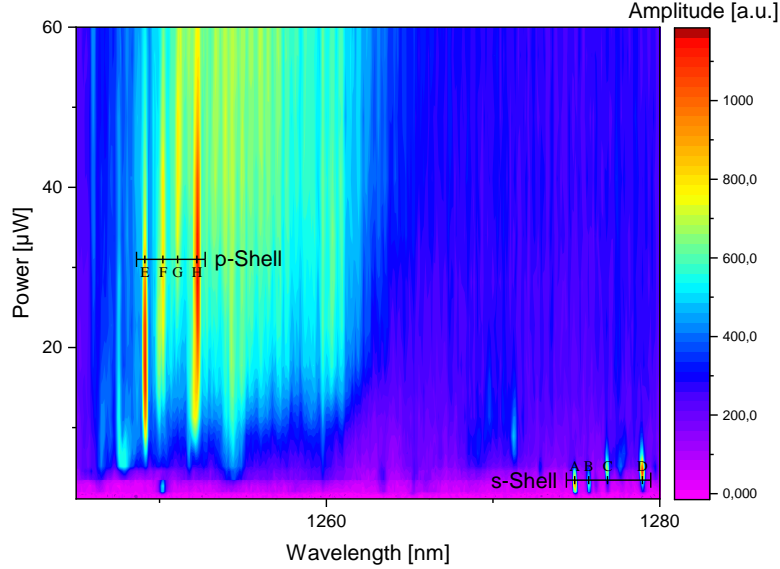

Figure 4.12: Plot of power vs. wavelength showing s- and p-shell. Four distinct peaks A, B, C, and D in the high wavelength region are marked at the power used for polarisation analysis. Analogously for peaks E, F, G, and H in the low wavelength region.

To further support this hypothesis we also investigate the power laws for those peaks and compare them. The resulting data with linear fits can be seen in Figure 4.13a and 4.13b. The slopes were again plotted in $\log_{10}$-$\log_{10}$-scale and linearly fitted in the low power region, i.e. the region where the respective peak starts to appear. The fits are again done until the data shows nonlinearities because of saturation.

For the s-shell we see the fits in Figure 4.13a. Peak A has a power dependency akin to a trion emission with slope $\sim 1{,}5$, while B as well as C both have a slope of around 2 indicating a biexciton. But peak D has a slope of around 2,5, which is neither typical (bi)excitonic nor trionic behaviour. An argumentation along the lines of the power law for trions in Section 4.2.1 can also be employed here: the state with $\mathcal{P} \propto \bar{n}^{2,5}$ could imply a biexciton or two excitons and one additional charge carrier (e.g. a *negative biexciton* XX^- or a *positive biexciton* XX^+). Take note that the slope values correlate with the peak's wavelength: the higher the wavelength the higher the slope. In total, the power law is not completely conclusive regarding the identification of the states and further analysis needs to be done like PLE to scan through the p-shell or polarisation dependent measurements (see Section 4.2.3).

The p-shell power dependency is shown in Figure 4.13b. Its complete characterisation including identification of transitions is not feasible with only the existing data[8] and out of the scope of this thesis, for p-shell states are more complicated than simple excitonic transitions. But nevertheless we may infer something of value regarding our postulated pairing $\{(A, E), (B, F), (C, G), (D, H)\}$. I again fit the peaks in their respective onset regions until they started to show saturation. The power laws in the p-shell are similar in structure as the s-shell. In the s-shell we have strictly monotonically increasing slopes for increasing wavelengths (cf. Fig. 4.13a). The same is true for E-H in Figure 4.13b: peak E at wavelength 1249,12 nm has the lowest slope of around 1,13 of the p-shell quadruplet, followed by F with $\sim 1,96$ at 1250,20 nm. G has a slope of $\sim 2,08$ at 1251,08 nm and finally H concludes the quadruplet with slope $\sim 2,28$ at 1252,24 nm. Even though we cannot really conclude anything about the specific transitions from this alone, it is still remarkable that this structure is also present here. This strengthens the claim that the peaks under consideration are indeed related. Not only this monotonically increasing relation between s-shell and p-shell emphasises this, but also the values of the slopes in the pairs. A nice juxtaposition of the values can be found in Table 4.1 which compares different characteristics of both s-shell and p-shell quadruplets regarding their power and polarisation behaviour.
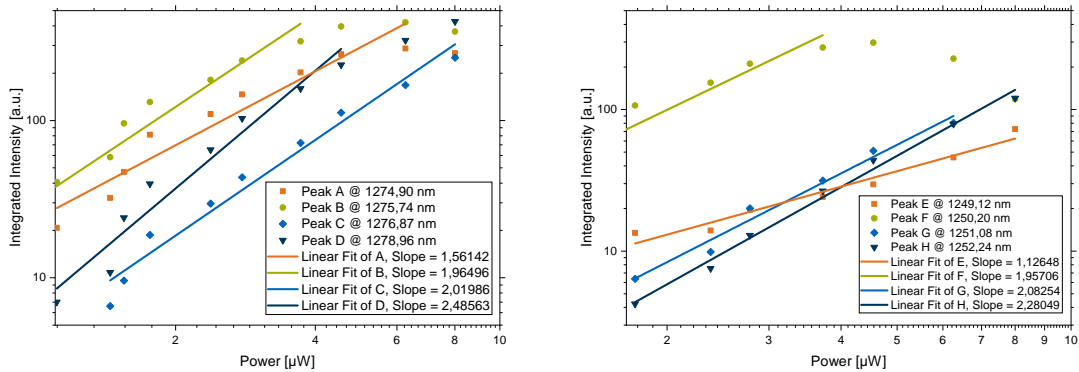
(a) Linear fit of integrated intensities of s-shell peaks A-D to show their power dependence.

(b) Linear fit of integrated intensities of p-shell peaks E-H to show their power dependence.

Figure 4.13: The power dependence of low and high energy peaks A-H in comparison.

---

[8]PLE measurements would help to investigate this further and would shed more light on the pairing $\{(A, E), (B, F), (C, G), (D, H)\}$.

Polarisation Dependence of Excitonic Transitions from s-Shell and p-Shell Energy States

The polarisation dependent measurements help us to identify transitions with more certainty also on the sample emitting in the O-band. But in contrast to the sample emitting in the C-band we not only investigate the peaks to gather information about the FSS of the different paths in the biexciton-exciton cascade. We also investigate the polarisation dependent behaviour of the postulated s-shell and p-shell states to gain more insight into them.

As we have seen in the last section the slope would lead us to believe that A is a trion which proved to be well-founded, as the peak is not really oscillating spectrally. No spectral oscillation means that we have a TLS which decays optically and without favouring a specific polarisation as it would be the case for a biexciton-exciton-cascade. This can be seen in Figure 4.14a. It also shows that B is oscillating with a numerically computed spectral shift of $2A = 0{,}041\,02\,\text{nm}$, that means it corresponds with our expectation from slope 2 that it is a biexciton. It also is roughly of the same order of magnitude calculated for the other spectral oscillations we had before on this sample.

Transition C on the other hand is more puzzling as it has also a slope of roughly 2 but it does not oscillate, which is clearly visible from Fig. 4.14a. Thus, it does not exhibit typical biexcitonic behaviour. So this seems to be another transition, because the slope is clearly around 2, which would indicate that two excitonic particles are involved in this transition. Regarding peak D we speculated before that it could be a charged biexciton because of its slope around 2,5. We also observe a spectral shift of $2A = 0{,}090\,32\,\text{nm}$ in our fit in Fig. 4.14a. While A and B may still be explained with the simple power law model in conjunction with investigations into FSS as before, C and D pose a problem. Thus, it seems like the simple power law model for low powers breaks down in this case. That means we have to have a look at more complex processes involving also the p-shell transitions.

Regarding the p-shell transitions we see in Figure 4.14b that both E and G are not oscillating, while F and H are. F exhibits a spectral shift of $2A = 0{,}031\,52\,\text{nm}$ which is still comparable to the shift of B, while H is also oscillating with higher amplitude resulting in a shift of $2A = 0{,}163\,66\,\text{nm}$ which is not only much more than the oscillations of F and B, but also substantially more than D.

We can suspect that for C and D but also for lines in the p-shell the slope model breaks down. We may in reality see the emissions from three or more excitons or complex charged states (*triexciton* 3X, *quadexciton* 4X, charged biexcitons $XX^{\pm}$). States with similar splitting mechanisms akin to biexciton-exciton cascade would result in spectral oscillations and emissions from charged states analogous to trionic states would not exhibit spectral oscillations. Or it could be that one line in the p-shell region and one line in the s-shell region stem

(a) Polarisation dependence of s-shell peaks A-D.
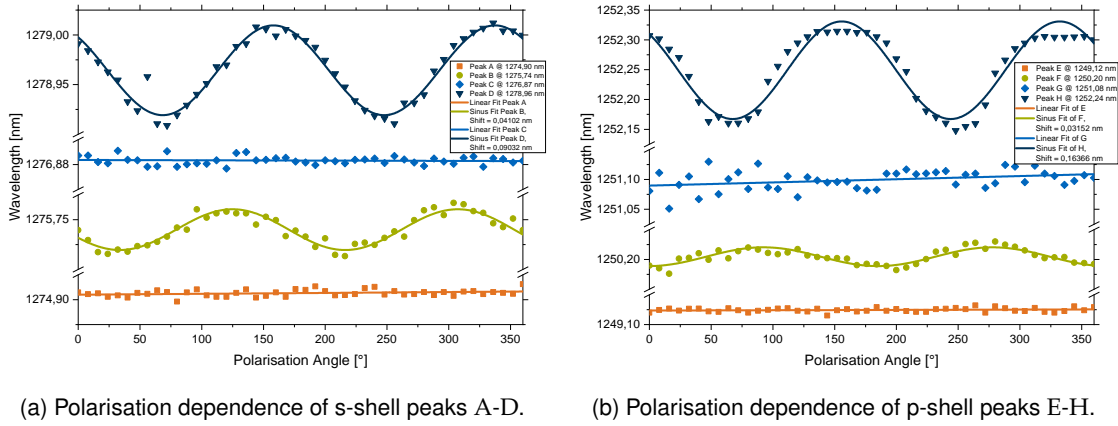
(b) Polarisation dependence of p-shell peaks E-H.

Figure 4.14: The polarisation dependence of low and high energy peaks A-H in comparison.

from one single cascade. For example, either C or D correspond to an e^- from the p-shell recombining to an h^+ in the s-shell. Additionally, one p-shell line of E to H would be a corresponding recombination of a hole s.t. the electron of the s-shell line would be in position to recombine.

For example, according to the energy structure of a negative biexciton described in [23] a charged biexciton could perhaps be the source of H, G, and D. As seen in Figure 4.15 a negative biexciton XX^- has an optically active two-path cascade (analogously to the biexciton-exciton cascade) from XX^- over two different split optically active trionic states X_{3T}^{-*} and X_{2T}^{-*} with additional e^- in the p-shell. These decay radiatively to a QD with only one e^- in the p-shell denoted 0^{-*} (this decays non-radiatively to a QD with e^- in the s-shell, denoted 0^-). This can be the source of the oscillation in D and H. The optical decay from XX^- to X_{4S}^{-*} which non-radiatively decays to the normal X^- could then be the source of non-oscillating G. But one can not easily explain the bigger amplitude of the oscillations in H compared to D in a rigorous fashion without further investigation. [23, p.20]

But similarly such emissions could perhaps also be explained via positive biexcitons or even doubly charged excitons (cf. [23, pp.21 et seqq.] for further information about their transitions) with only the existing data. As such this should only be regarded as a *Denkanstoß*, which shows that those transitions are much more complex than the (bi-)excitonic and trionic ones we discussed before.

Even though the oscillations may differ in phase and amplitude and the nature of their relation remains unclear, the existence of a relation of s-shell transitions and p-shell transitions remains apparent. I compiled a concise summary of the different characteristics for pairs (A, E), (B, F), (C, G), and (D, H) which can be found line-wise in Table 4.1 for easy comparison.
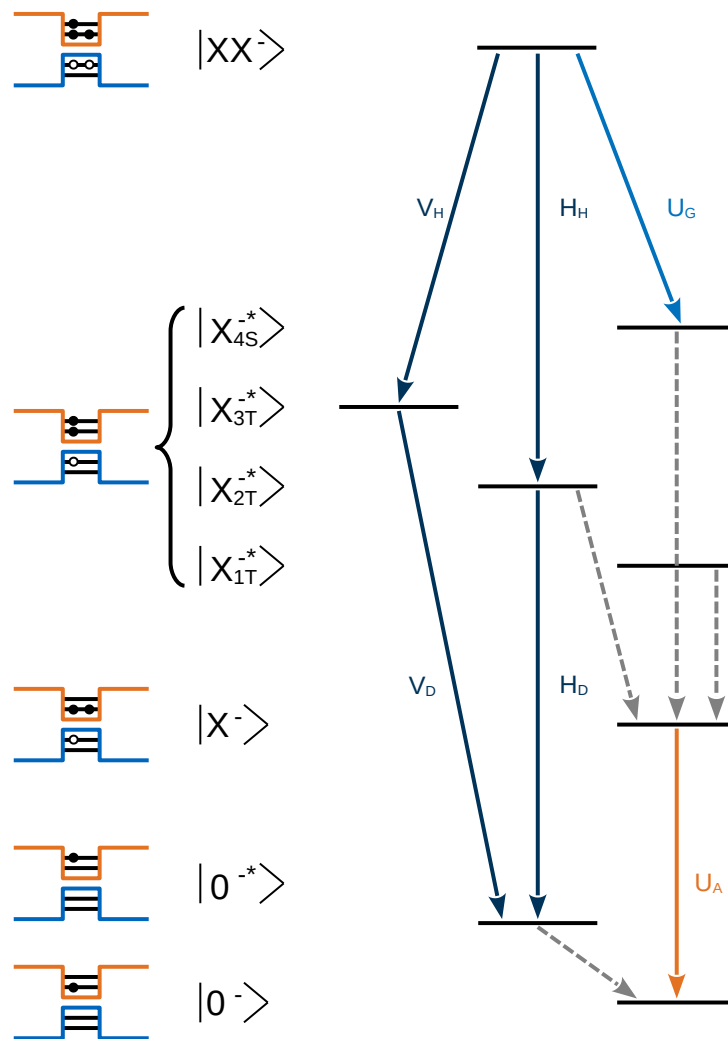
Figure 4.15: Energy structure for possible explanation of some of the behaviour in p- and s-shell. Suspected optically active transitions are labelled with vertical V, horizontal H or undetermined polarisation U, which may be from the peak given as a subscript. Relaxation processes are denoted by grey arrows. The electronic configuration of the different states (names and spin configurations as in [23]) is given schematically on the left, where e^- in the CB are represented with filled circles and h^+ in the VB denoted as empty ones. Adapted from [23, p.20].

Thus, we conclude that a relation between those emissions seems to exist in whichever form.

Table 4.1: Comparison of power and polarisation characteristics of s-shell emission quadru-
plet (A, B, C, D) and p-shell emission quadruplet (E, F, G, H).

	s-Shell					p-Shell			
ID	λ [nm]	Slope	$2A$ [nm]	Source	ID	λ [nm]	Slope	$2A$ [nm]	Source
A	1274,90	1,561	-	$X^{\pm}$	E	1249,12	1,126	-	?
B	1275,74	1,965	0,041 02	XX	F	1250,20	1,957	0,031 52	?
C	1276,87	2,020	-	?	G	1251,08	2,083	-	XX^- ?
D	1278,96	2,486	0,090 32	XX^- ?	H	1252,24	2,280	0,163 66	XX^- ?

Therefore, we recommend further investigation with a PLE experiment to study the relation of
s-shell and p-shell emissions. Also identification of excitonic transitions in the s-shell is not
established with absolute certainty either, even though our results strongly show this. But
PLE data would clarify this beyond any doubt. In PLE it would be possible to excite p-shell
transitions which then will also decay into the corresponding s-shell states which should clear
up their relation.

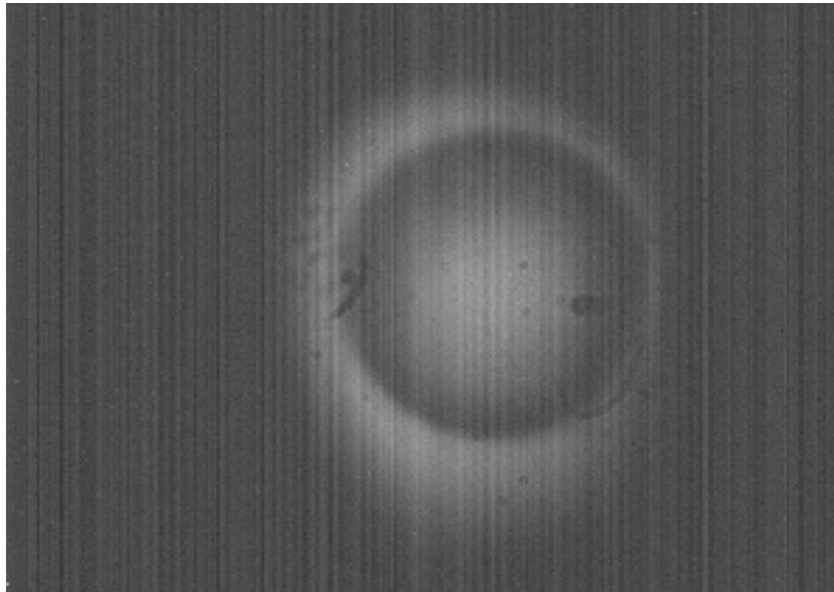### 4.2.4 Solid Immersion Lenses on the Sample Emitting in the O-Band

Figure 4.16: A SIL with $50\,\mu\text{m}$ diameter imaged with the *Bobcat* camera and the $1050\,\text{nm}$
imaging LED. The area of the sample given by the FoV of the imaging system is
also visible. It is slightly larger than the SIL.

Now we investigate the hemispherical SILs grown on the sample by Björn Jonas. An image

of such a SIL can be seen in Figure 4.16. It was captured with the *Bobcat* camera and the 1050 nm imaging LED. The illuminated area of the sample – i.e. the area given by the FoV of the imaging system – shows a 50 μm diameter SIL. The confines of the FoV are also clearly visible around the edge of the SIL, which implies that it is slightly larger than 50 μm.

As mentioned in Section 2.3.3 the hemispherical SILs on the sample emitting in the O-band have refractive index $n_{SIL} \approx 1{,}515$. [38] With the additional parameter n_{Host} of the sample the collection efficiency, i.e. the proportion of the QD emission which is going to the objective can be simulated. Such a simulation can be seen in Figure 4.17. For the refractive index of the sample $n_{Host} = 3{,}57$ was used which is a value calculated from the empirical *Sellmeier equation* [59] for 300 K and 1320 nm for $In_{0.32}Ga_{0.68}As$ (top surface of the MBL). [60, 61] This is only a rough estimate as the SILs on this sample would actually work at low temperature and with $In_{0.18}Ga_{0.82}As$ which is the top surface of the sample, but the top of the MBL needs to be considered for a simulation in case of a DBR underneath. By this estimation the simulation should also give an idea for future samples with DBR, but is not really far off from what is expected from this sample. The calculations include a baseline simulation for the sample without SIL (black lines in Fig. 4.17), with hemispherical (orange lines in Fig. 4.17), and hyperhemispherical SILs (blue lines in Fig. 4.17). The collection efficiencies are calculated both with angle-dependent *Fresnel equations* (solid lines in Fig. 4.17) and with a simplified version, which always assumes normal incidence of light beams on the SIL's surface (dashed lines in Fig. 4.17). The NA of the objective of $\sim 0{,}81$ [55] is marked with a grey dashed line and the intersections with the graphs would give the supremum of achievable efficiency with this NA under our model assumptions. Without SILs that would only be $\sim 1{,}25\,\%$ while with hemispherical SILs we get around $3{,}25\,\%$ to $3{,}5\,\%$ for the different models, which is an improvement of almost factor 3. The simplified model for hyperhemispheres shows even more than $5{,}25\,\%$, but the more realistic Fresnel model tops out at roughly $4\,\%$. This is still some improvement over hemispheres in case of our objective, but this improvement probably does not warrant the more involved fabrication of hyperhemispheres for now. Because of this we investigate the effect of hemispheres in this thesis. Hyperhemispheres could be an option for further improvements in the future.

As we are not able to measure the real collection efficiency directly, we compare spectra captured with and without SILs and then compare the different diameters to the baseline measurements. This way we can show that the SILs actually work and also quantify how well. This way we can find the sweet spot for hemispherical SIL diameter (at least from the limited selection we have). The SILs on our sample are not grown over a specific QD in the centre of it. Thus, we do not want to compare single emission peaks in this experiment. We look at the ensemble emissions from the different SILs. To do this we use the laser excitation at 785 nm at a fixed excitation power. This way we measure the spectra in the O-band at a power of $\sim 1{,}19\,μW$. In Figure 4.18 we can compare the average emissions of the sample for the different SIL diameters. For each SIL the focus and x- and y-positions
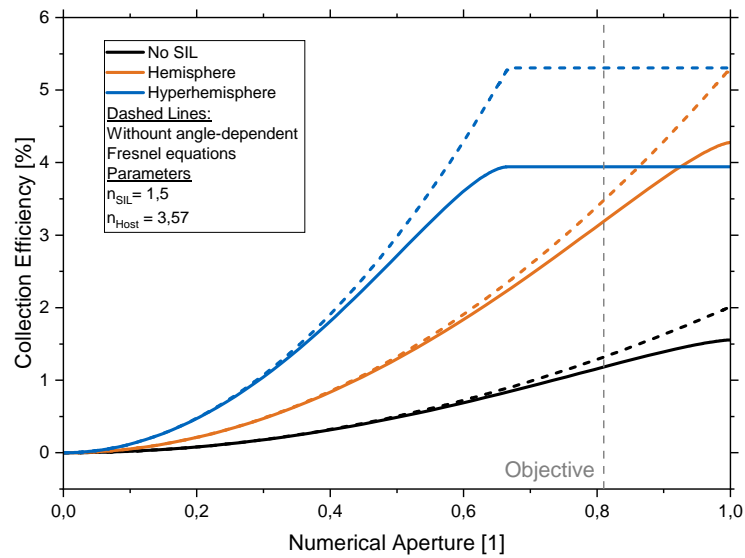
Figure 4.17: Simulation of the collection efficiency of hemispherical, hyperhemispherical, and no SILs for the material parameters of our sample vs. NA. The NA of the objective is marked. Simulation courtesy of Björn Jonas.

were optimised, s.t. the emissions were maximal for the central position of the respective SIL under consideration. Afterwards the average of the emission for each row of different diameters was calculated. As the SILs are placed relatively close to each other the QD density for the different spots should be comparable and with the averaging differences stemming from noise, the QD density and manufacturing tolerances between different SILs are minimised. The averages were smoothed with Locally Estimated Scatterplot Smoothing (LOESS) and then the maximum was taken to quantify the performance of the respective SIL diameter. It is clear from Figure 4.18, every diameter of SIL works as intended and is thus better than the baseline (black in Fig. 4.18), but we also see that $25\,\mu m$ SILs (dark blue in Fig. 4.18 with $\sim 133{,}1\,\%$ relative performance) are worse than $50\,\mu m$ SILs (lighter blue in Fig. 4.18 with $\sim 146{,}1\,\%$ relative performance), but higher diameters like $100\,\mu m$ SILs (green in Fig. 4.18 with $\sim 133{,}5\,\%$ relative performance) and $200\,\mu m$ SILs (orange in Fig. 4.18 with $\sim 126{,}0\,\%$ relative performance) result in gradually worse performance. This suggests, that the optimal performance of SILs in this case is around $50\,\mu m$ in diameter. Further optimisation could be achieved by a less limited sample size of diameters in the range from $25\,\mu m$ to $100\,\mu m$ to track down the location of the maximum more precisely. To boost the performance of one individual QD the position of the SIL could be optimised by searching for a very bright QD in the desired spectral region with a combination of wide-field microscopy or Macro-Photoluminescence (Macro-PL) (to identify bright QDs on a big area of the sample) and subsequent µPL to investigate the spectral characteristics. Afterwards the SIL of optimal diameter (to be determined first, of course) could be fabricated on top.
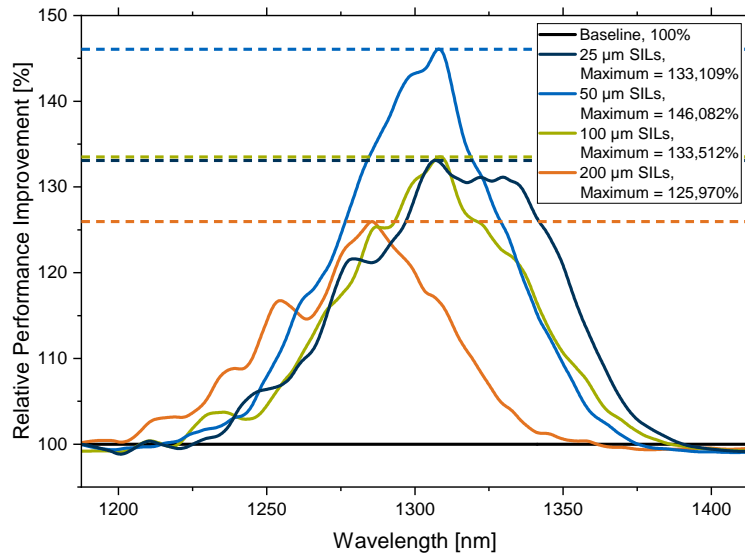
Figure 4.18: Impact of SIL diameter on the emission performance in the O-band region. The relative performance is measured as the maximum of the LOESS smoothed average over each diameter of the emission strength with the SILs w.r.t. the average of the baseline measurements without them.

In total it is to say that the SILs definitely work and are a simple method of improving the collection efficiency on samples like ours.

5 Conclusion

To recapitulate, we built an experimental setup for µPL measurements to investigate the power dependent and polarisation dependent behaviour of single InAs QDs on GaAs substrate with graded $\mathrm{In_{1-x}Ga_xAs}$ MBL emitting in the C-band which were grown with MOVPE and MBE grown samples with MBL emitting in the O-band. We performed such measurements on both types of samples and investigated emissions from biexciton-exciton cascades, their FSS and DOLP. Furthermore, we examined s-shell and p-shell states from the sample emitting in the O-band and preliminarily identified some transitions. In addition, we also performed comparative measurements on ensemble emissions from the sample emitting in the O-band with and without SILs and determined the relative performance improvement of different SIL diameters.

5.1 Outlook on Further Experiments

For the future we suggest PLE measurements to study the relation between s-shell and p-shell emissions more closely, which may lead to the development of optical p-shell excitation schemes. To show the quantum nature of the emissions from such QDs the next steps would include measurements of $g^{(2)}(0)$. The foundations for widefield microscopy on the samples are also already in place, which improves the efficiency of using the setup to find bright QDs and in turn do statistical analysis of $\mathrm{i.a.}$ FSS for many different QDs. As an outlook, it would also be beneficial to study p-shell states via pulsed excitation – i.e. time resolved – measurements.

5.2 Future Sample Optimisation

The ideal future samples for applications like QKD may include optimisations like the following:

- A DBR underneath, maybe coupled with another cavity design around bright QDs if possible, in order to boost collection efficiency.

- Optimised QD growth temperature to minimise FSS and thus enhancing the degree of entanglement of generated photon pairs.

- Optimised hemispherical SIL diameter and position to further boost collection efficiency, or even using hyperhemispherical ones for the last bit of collection efficiency when needed.

- And probably many more.

5.3 Final Remarks

To conclude, QDs emitting in the telecommunication wavelength range, especially in the C-band and O-band are not only feasible but show great potential moving forward to long-range QKD systems and other applications in quantum communication and quantum information processing. In particular the novel MBE grown InAs QDs on a GaAs substrate with graded $\mathrm{In_{1-x}Ga_xAs}$ MBL emitting in the O-band look very promising for this purpose, because they have low absorption in commonly used fibre-optics and no wavepacket dispersion. Even without optimisations the performance looks good and it can be improved via optimisations of growth parameters, SILs and a suite of cavity designs. Nevertheless more research into the generated emissions should be conducted. This may be connected with development of optically driven excitation schemes utilising p-shell states for driving single photon generation via excitonic states and/or entangled photon pair generation via biexciton-exciton cascade. The implementation of optical excitation schemes in p-shell energy levels could provide additional ways of generation of entangled photon pairs, which may be advantageous for specific applications. Such QDs can be a step into the direction of deterministic, high-performance and high-efficiency quantum light sources for large scale applications in the telecom range.

List of Figures

List of Figures

List of Tables

Glossary

Entries with superscripts [a] and [b] are taken from [62] and [6] respectively.

(Linear) Operator A (linear) mapping, which can be used to create new mathematical objects from others (e.g. $+$, $-$, ∇, matrices, etc.). In quantum mechanics operators – there commonly denoted with a hat ˆ – operate on quantum states like (potentially infinite-dimensional) matrices on vectors in order to measure the quantity associated with it (cf. glossary entry on Observable). E.g. position/momentum operator $\hat{x}/\hat{p}$ to measure position/momentum or the Hamilton operator $\hat{H}$ to measure energy.

Achromat Optics which limits the effects of spherical and chromatic aberrations. Its improved version is the apochromat.

Anisotropy Opposite of isotropy, i.e. different properties in different dimensions.

Apochromat Optics which almost eliminates the effects of spherical and chromatic aberrations. It is the improved version of the achromat.

Banach Space A complete vector space on which a norm can be defined.

Basis[a] A minimal set of vectors of a vector space which is able to determine the position of every point in it via a linear combination. Every vector in a basis is called basis vector.

Coherence Describes the correlation of frequency or phase of one wave with another wave or of one part of one wave with another part of the same wave. Impacts the ability of a wave to interfere with other waves or itself.

Coherence Time Describes the time scale for how long a wave is coherent.

Degeneracy Existence of two or more measurable quantum states with the same energy level. In other words, there exist more than one linearly independent eigenstates with the same eigenvalue of an observable.

Degree of Freedom[a] Independent and variable parameter which can be chosen freely, i.e. without affecting other DoF. A set of parameters/DoF uniquely determine a system.

Dimension[a] Number of DoF in a space or the magnitude of a vector spaces' basis. Notation: $|B| = dim(V)$ gives the dimension of vector space V with basis B.

Discreteness[a] Something having enumerable many states with non-continuous transitions and well-defined magnitudes. E.g. quantised physical quantities, digital signals or integer numbers are discrete.

Eigenfunction A function f satisfying the eigenvalue problem $\mathbf{A}f = \lambda f$ with operator $\mathbf{A}$ and eigenvalue λ.

Eigenstate Eigenvector or more generally eigenfunction corresponding to an eigenvalue of a quantum mechanical operator.

Eigenvalue Problem In linear algebra the **(special) Eigenvalue Problem** is the problem of solving the **Eigenvalue Equation** $\mathbf{A}\vec{v} = \lambda\vec{v}$, where $\mathbf{A}$ is a matrix (operator), $\vec{v}$ an **Eigenvector** and λ its corresponding **Eigenvalue**.

Entropy Measure of "disorder" or "ignorance" often denoted S or H. Comes in different forms like e.g. thermodynamic **Clausius-**, **Gibbs-** or **Boltzmann entropy**, quantum mechanical **von Neumann entropy** or the unifying information theoretical **Shannon entropy**.

Hilbert Space A Banach space with a norm induced by a scalar product.

Isotropy Opposite of anisotropy, i.e. the same properties in every dimension.

Linear Combination[a] Applying the superposition principle to mathematical constructs, where it is allowed, e.g. additions or scaling of vectors or wave functions.

Linear Independence[a] Property of a set of vectors. Vectors are linearly independent, if no vector in the set except the zero-vector ($\vec{0} = (0, 0, ..., 0)^T$ where $dim(\vec{0})$ is the dimension of the corresponding vector space) can be written as a nontrivial linear combination of others. I.e. no linear combination of vectors can describe the zero-vector except by setting all coefficients to 0.

Linearity[a] The property of fulfilling the superposition principle, i.e. construction of linear combinations is allowed.

Macro-Photoluminescence PL experiments carried out for a macro scale, e.g. a whole wafer or a comparably big part of a sample. Counterpart to micro-photoluminescence.

Micro-Photoluminescence PL experiments carried out for a micrometer scale section of a sample. Counterpart to macro-photoluminescence.

Multi-Mode Optical Fibre Optical fibre which can carry multiple modes – i.e. solutions of the electromagnetic wave equation (cf. **Maxwell Equations**, **Helmholtz Equation**) – of the light beam due to a high core diameter. This limits the maximal length of transmission due to different propagation speeds of modes. Counterpart to the single-mode optical fibre.

Observable A measurable quantity, in quantum mechanics connected with a corresponding operator acting on states in the state space of the system.

One-time pad[a] Symmetric encryption scheme providing perfect secrecy. Encryption of a message is done by modular addition over a finite field of a uniformly random, secret, single-use key which is at least as long as the message. Sometimes also called **Vernam cipher**.

Post-Quantum Cryptography[a] Part of cryptography dealing with algorithms secure against attacks with a quantum computer.

Prime Factorisation[a] Finding the prime factors of an integer number.

Pseudo-Random Number Generator[a] A generator for numbers, whose output is not distinguishable from a number randomly chosen from a given probability distribution. The output is dependent on the input value (called **seed**) in a deterministic and thus only *pseudo*-random fashion.

Pure State A quantum state which cannot be written as a mixture of others.

Quantum Bit[b] Basic unit of information in quantum information theory, abbreviated as qubit or qbit. The information contained in it is described as a (coherent) superposition of the wave function for the 0-state and 1-state of the respective physical construct carrying the information, e.g. a particle.

Quantum Cryptography[b] Utilising principles of quantum mechanics to perform cryptography.

Quantum Dot An accumulation of atoms, which act like only one atom quantum mechanically, i.e. the wave function is confined in all three spatial DoF (hence dot/pointlike or "0-dimensional" quantum structure). Similar concepts include **Quantum Wires** (confinement in 2 DoF, thus 1D) and **Quantum Wells** (confinement in 1 DoF, thus 2D).

Quantum Entanglement[a] Dependence of the quantum states of two or more particles which may or may not be separated by an arbitrary distance, where it is impossible to (fully) describe the quantum state of each particle separately.

Quantum Key Distribution[b] Utilising quantum mechanics to distribute a cryptographic key.

Quantum State State of a quantum mechanical system. Mathematically described by its corresponding wave function or via a vector corresponding to an observable.

Scytale[a] Transposition cipher using strips of inscribable media (e.g. leather, parchment or paper) wrapped around a (wooden) cylinder before writing a message on it. The cylinders' diameter constitutes the cryptographic key.

Single-Mode Optical Fibre Optical fibre which only carries a single transverse mode – i.e. the solution of the electromagnetic wave equation (cf. **Maxwell Equations**, **Helmholtz Equation**) oscillating perpendicular to the beam's propagation direction – of the light beam. Counterpart to the multi-mode optical fibre.

Steganography[a] Art of concealment or concealed transmission of information.

Superposition Principle[a] Main criterion of linearity. Combination of additivity and homogeneity properties.
$Additivity : f(x_1) + f(x_2) = f(x_1 + x_2)$
$Homogeneity : af(x) = f(ax).$

Superposition[a] A linear combination according to the superposition principle. In case of quantum mechanics: additions and scaling of multiple wave functions or quantum states.

True Random Number Generator[a] A generator for numbers, whose output is a number randomly chosen from a given probability distribution. The output is dependent on e.g. unpredictable physical processes/fluctuations like statistically random thermal noise or the like, and **not** on the input value to an algorithm, which would be the case in a Pseudo-Random Number Generator. It can be considered non-deterministic and "truly" random.

Unitary Transformation[a] A transformation preserving the inner product. It is linear (see linearity and superposition principle), injective, congruent (distance-preserving) and norm-preserving.

Vector Space[a] A space spanned by a specified number of linearly independent basis vectors (see linear independence), where every point in this space can be described via a linear combination of them. It is uniquely determined by one of arbitrarily many bases.

Wave Equation[a] Differential equation governing the propagation of waves in general. It is the equation of motion in quantum mechanical contexts; often **Schrödinger's equation**.

Wave Function[a] A function solving the wave equation. In quantum mechanics it is used to describe a quantum state mathematically. The square of its absolute value is the probability density function of that state. This means exemplary for one particle: it determines the probability of a particles location or momentum – if the wave function is given in the position space or momentum space respectively.

Acronyms

In this section used acronyms are listed.

µPL Micro-Photoluminescence.

AR Anti-Reflective.

BBO Beta Barium Oxide.

BS Beam Splitter.

CB Conduction Band.

CCD Charge-Coupled Device.

CTL Continuously Tunable Laser.

DBR Distributed Bragg Reflector.

DFT Discrete Fourier Transformation.

DoF Degree of Freedom.

DOLP Degree of Linear Polarisation.

DW Dispersion Window.

EL Electroluminescence.

FAB Fibre Attenuator Box.

FoV Field of View.

FSS Fine Structure Splitting.

FT Fourier Transform.

FWHM Full Width at Half Maximum.

FWM Four Wave Mixing.

IR Infrared.

ISO International Organization for Standardization.

LED Light Emitting Diode.

LOESS Locally Estimated Scatterplot Smoothing.

Macro-PL Macro-Photoluminescence.

MBE Molecular Beam Epitaxy.

MBL Metamorphic-Buffer Layer.

MEMS Micro-Electro-Mechanical System.

MMF Multi-Mode Optical Fibre.

MOVPE Metal-Organic Vapor-Phase Epitaxy.

NA Numerical Aperture.

NIR Near-Infrared.

OTP One-Time Pad.

PL Photoluminescence.

PLE PL Excitation.

PM Polarisation Maintaining.

PPKTP Periodically Poled Potassium Titanyl Phosphate.

PQC Post-Quantum Cryptography.

QC Quantum Cryptography.

QD Quantum Dot.

QFT Quantum Fourier Transformation.

QKD Quantum Key Distribution.

qubit Quantum Bit.

RF Resonance Flourescence.

SIL Solid Immersion Lens.

SMF Single-Mode Optical Fibre.

SNR Signal-to-Noise Ratio.

SPDC Spontaneous Parametric Down Conversion.

SPS Single-Photon Source.

TEM Transmission Electron Microscope.

TLS Two-Level System.

TRNG True Random Number Generator.

UHV Ultra-High Vacuum.

UV Ultraviolet.

VB Valence Band.

VIS Visible.

WDM Wavelength Division Multiplexing.

WL Wetting Layer.

References

[1] C. E. Shannon. "Communication theory of secrecy systems". In: *The Bell System Technical Journal* 28.4 (1949), pp. 656–715. DOI: 10.1002/j.1538-7305.1949.tb00928.x.

[2] C. E. Shannon. "A mathematical theory of communication". In: *The Bell System Technical Journal* 27.3 (1948), pp. 379–423. DOI: 10.1002/j.1538-7305.1948.tb01338.x.

[3] M. A. Nielsen and I. L. Chuang. *Quantum Computation and Quantum Information: 10th Anniversary Edition*. Cambridge University Press, Dec. 2010. ISBN: 9781107002173. DOI: 10.1017/CBO9780511976667.

[4] M. D. Schwartz. *Lecture Notes in Statistical Mechanics, Spring 2021*. https://scholar.harvard.edu/files/schwartz/files/physics_181_lectures.pdf, Last Access: 16.11.2022.

[5] W. Heisenberg. "Über den anschaulichen Inhalt der quantentheoretischen Kinematik und Mechanik". In: *Zeitschrift für Physik* 43.3 (Mar. 1927), pp. 172–198. ISSN: 0044-3328. DOI: 10.1007/BF01397280. URL: https://doi.org/10.1007/BF01397280.

[6] P. Kohl. *Quantum Cryptography*. Seminar Report in Advanced Topics in Quantum Computing at the Department of Informatics of Technical University of Munich. Nov. 2021.

[7] C. H. Bennett and G. Brassard. "Quantum cryptography: Public key distribution and coin tossing". In: *Theoretical Computer Science* 560 (2014). Theoretical Aspects of Quantum Cryptography – celebrating 30 years of BB84, pp. 7–11. ISSN: 0304-3975. DOI: https://doi.org/10.1016/j.tcs.2014.05.025. URL: https://www.sciencedirect.com/science/article/pii/S0304397514004241.

[8] R. P. Feynman. "Simulating physics with computers". In: *International Journal of Theoretical Physics* 21.6 (June 1982), pp. 467–488. ISSN: 1572-9575. DOI: 10.1007/BF02650179. URL: https://doi.org/10.1007/BF02650179.

[9] P. W. Shor. "Polynomial-Time Algorithms for Prime Factorization and Discrete Logarithms on a Quantum Computer". In: *SIAM Journal on Computing* 26.5 (Oct. 1997), pp. 1484–1509. ISSN: 1095-7111. DOI: 10.1137/s0097539795293172. URL: https://dx.doi.org/10.1137/S0097539795293172.

References

[10]   R. L. Rivest, A. Shamir, and L. Adleman. "A method for obtaining digital signatures and public-key cryptosystems". In: *Communications of the ACM* (1978).

[11]   X. Tan. "Introduction to Quantum Cryptography". In: *Theory and Practice of Cryptography and Network Security Protocols and Technologies*. Ed. by J. Sen. Rijeka: IntechOpen, 2013. Chap. 5. DOI: 10.5772/56092. URL: https://doi.org/10.5772/56092.

[12]   A. K. Ekert. "Quantum cryptography based on Bell's theorem". In: *Phys. Rev. Lett.* 67 (6 Aug. 1991), pp. 661–663. DOI: 10.1103/PhysRevLett.67.661. URL: https://link.aps.org/doi/10.1103/PhysRevLett.67.661.

[13]   Mark Fox. *Quantum Optics: An Introduction*. Vol. 15. Oxford Master Series in Physics. Oxford University Press, 2006. ISBN: 9780198566724.

[14]   K. Zeuner. "Semiconductor Quantum Optics at Telecom Wavelengths". PhD thesis. KTH, Quantum and Biophotonics, 2020. ISBN: 978-91-7873-689-8. URL: http://urn.kb.se/resolve?urn=urn%3Anbn%3Ase%3Akth%3Adiva-285782.

[15]   M. Anderson, T. Müller, J. Huwer, J. Skiba-Szymanska, A. B. Krysa, R. M. Stevenson, J. Heffernan, D. A. Ritchie, and A. J. Shields. "Quantum teleportation using highly coherent emission from telecom C-band quantum dots". In: *npj Quantum Information* 6.1 (Jan. 2020), p. 14. ISSN: 2056-6387. DOI: 10.1038/s41534-020-0249-5. URL: https://doi.org/10.1038/s41534-020-0249-5.

[16]   P. A. M. Dirac and R. H. Fowler. "The physical interpretation of the quantum dynamics". In: *Proceedings of the Royal Society of London. Series A, Containing Papers of a Mathematical and Physical Character* 113.765 (1927), pp. 621–641. DOI: 10.1098/rspa.1927.0012. eprint: https://royalsocietypublishing.org/doi/pdf/10.1098/rspa.1927.0012. URL: https://royalsocietypublishing.org/doi/abs/10.1098/rspa.1927.0012.

[17]   M. Volmer and A. Weber. "Keimbildung in übersättigten Gebilden". In: *Zeitschrift für Physikalische Chemie* 119U.1 (1926), pp. 277–301. DOI: doi:10.1515/zpch-1926-11927. URL: https://doi.org/10.1515/zpch-1926-11927.

[18]   I. N. Stranski and L. Krastanow. "Zur Theorie der orientierten Ausscheidung von Ionenkristallen aufeinander". In: *Monatshefte für Chemie und verwandte Teile anderer Wissenschaften* 71 (1 1937), pp. 351–364. DOI: 10.1007/BF01798103. URL: https://doi.org/10.1007/BF01798103.

[19]   F. C. Frank and J. H. van der Merwe. "One-dimensional dislocations. I. Static theory". In: *Proceedings of the Royal Society A* 198 (1053 1949). DOI: 10.1098/rspa.1949.0095. URL: https://doi.org/10.1098/rspa.1949.0095.

[20]   F. C. Frank and J. H. van der Merwe. "One-dimensional dislocations. II. Misfitting monolayers and oriented overgrowth". In: *Proceedings of the Royal Society A* 198 (1053 1949). DOI: 10.1098/rspa.1949.0096. URL: https://doi.org/10.1098/rspa.1949.0096.

[21] F. C. Frank and J. H. van der Merwe. "One-dimensional dislocations - III. Influence of the second harmonic term in the potential representation, on the properties of the model". In: *Proceedings of the Royal Society A* 200 (1060 1949). DOI: 10.1098/rspa.1949.0163. URL: https://doi.org/10.1098/rspa.1949.0163.

[22] L. De Broglie. "Recherches sur la théorie des Quanta". In: *Ann. Phys.* 10.3 (1925), pp. 22–128. DOI: 10.1051/anphys/192510030022. URL: https://doi.org/10.1051/anphys/192510030022.

[23] S. Gordon. "Einzelne Quantenpunkte in elektrisch abstimmbaren Diodenstrukturen: Photolumineszenz und kohärente Photostromspektroskopie". 2017. DOI: 10.17619/UNIPB/1-258. URL: https://nbn-resolving.org/urn:nbn:de:hbz:466:2-30086.

[24] R. J. Young, R. M. Stevenson, A. J. Shields, P. Atkinson, K. Cooper, D. A. Ritchie, K. M. Groom, A. I. Tartakovskii, and M. S. Skolnick. "Inversion of exciton level splitting in quantum dots". In: *Phys. Rev. B* 72 (11 Sept. 2005), p. 113305. DOI: 10.1103/PhysRevB.72.113305. arXiv: quant-ph/0601198 [quant-ph]. URL: https://link.aps.org/doi/10.1103/PhysRevB.72.113305.

[25] D. Gabor. "Theory of communication. Part 1: The analysis of information". English. In: *Journal of the Institution of Electrical Engineers - Part III: Radio and Communication Engineering* 93 (26 Nov. 1946), 429–441(12). ISSN: 0367-7540. DOI: 10.1049/ji-3-2.1946.0074. URL: https://digital-library.theiet.org/;jsessionid=171ani3a0mk4u.x-iet-live-01content/journals/10.1049/ji-3-2.1946.0074.

[26] E. Zubko and E. Chornaya. "On the Ambiguous Definition of the Degree of Linear Polarization". In: *Research Notes of the AAS* 3.3 (Mar. 2019), p. 45. DOI: 10.3847/2515-5172/ab0c11. URL: https://dx.doi.org/10.3847/2515-5172/ab0c11.

[27] P. Wyborski, P. Podemski, P. A. Wroński, F. Jabeen, S. Höfling, and G. Sęk. "Electronic and Optical Properties of InAs QDs Grown by MBE on InGaAs Metamorphic Buffer". In: *Materials* 15.3 (2022). ISSN: 1996-1944. DOI: 10.3390/ma15031071. URL: https://www.mdpi.com/1996-1944/15/3/1071.

[28] *ISO 20473:2007*. ISO Standard 20473:2007 Optics and photonics — Spectral bands https://www.iso.org/standard/39482.html, Last Access: 23.02.2023.

[29] E. F. Schubert. *Light-Emitting Diodes*. 3rd ed. E. F. Schubert, 2018. ISBN: 0986382663.

[30] R. Ramaswami. "Optical fiber communication: from transmission to networking". In: *IEEE Communications Magazine* 40.5 (2002), pp. 138–147. DOI: 10.1109/MCOM.2002.1006983.

[31] J. R. Howell, K. J. Daun, R. Siegel, and M. P. Mengüç. *Thermal radiation heat transfer*. Seventh. CRC Press, 2021. ISBN: 9781000257816.

[32] S. L. Portalupi, M. Jetter, and P. Michler. "InAs quantum dots grown on metamorphic buffers as non-classical light sources at telecom C-band: a review". In: *Semiconductor Science and Technology* 34.5 (Apr. 2019), p. 053001. DOI: `10.1088/1361-6641/ab08b4`. URL: `https://dx.doi.org/10.1088/1361-6641/ab08b4`.

[33] F. Grünenfelder, R. Sax, A. Boaron, and H. Zbinden. "The limits of multiplexing quantum and classical channels: Case study of a 2.5 GHz discrete variable quantum key distribution system". In: *Applied Physics Letters* 119.12 (2021), p. 124001. DOI: `10.1063/5.0060232`. arXiv: `quant-ph/arXiv:2109.02412 [quant-ph]`. URL: `https://doi.org/10.1063/5.0060232`.

[34] M. B. Ward, O. Z. Karimov, D. C. Unitt, Z. L. Yuan, P. See, D. G. Gevaux, A. J. Shields, P. Atkinson, and D. A. Ritchie. "On-demand single-photon source for 1.3µm telecom fiber". In: *Applied Physics Letters* 86.20 (2005), p. 201111. DOI: `10.1063/1.1922573`. eprint: `https://doi.org/10.1063/1.1922573`. URL: `https://doi.org/10.1063/1.1922573`.

[35] B. Scaparra, A. Ajay, P. Avdienko, X. Yuyang, H. Riedl, P. Kohl, B. Jonas, B. Costa, E. Sirotti, P. Schmiedeke, V. Villafañe, I. D. Sharp, G. Koblmüller, J. J. Finley, and K. Müller. "Structural properties of graded $In_xGa_{1-x}As$ metamorphic buffer layers for quantum dots emitting in the telecom bands". In preparation.

[36] A. Cho and J. Arthur. "Molecular beam epitaxy". In: *Progress in Solid State Chemistry* 10 (1975), pp. 157–191. ISSN: 0079-6786. DOI: `https://doi.org/10.1016/0079-6786(75)90005-9`. URL: `https://www.sciencedirect.com/science/article/pii/0079678675900059`.

[37] B. Jonas, A. Zrenner, and S. Schumacher. "Two-Photon Physics with Biexcitons in single Quantum Dots". 2022. DOI: `10.17619/UNIPB/1-1636`. URL: `https://nbn-resolving.org/urn:nbn:de:hbz:466:2-43973`.

[38] *nanoscribe IP-S Photoresist Specifications*. `https://www.nanoscribe.com/en/products/ip-photoresins/#tab-15624`, Last Access: 21.03.2023.

[39] *attocube attoDRY800 Specification*. `https://www.attocube.com/downloads/attodry800.pdf`, Last Access: 11.01.2023.

[40] *Newport S-2000A Product Page*. `https://www.newport.com/f/pneumatic-vibration-isolators-with-automatic-re-leveling`, Last Access: 01.02.2023.

[41] *Thorlabs V800PA Fibre Attenuator Specifications*. `https://www.thorlabs.com/drawings/3dd7e3d0daed070f-80851851-ECB2-1BD8-EF669C045D8E0D65/V800PA-SpecSheet.pdf`, Last Access: 01.02.2023.

[42] *Thorlabs V1000PA Fibre Attenuator Specifications*. `https://www.thorlabs.com/drawings/5150eaa977186aa4-29762C10-FB67-D411-606E63FDB3E0FB14/V1000PA-SpecSheet.pdf`, Last Access: 01.03.2023.

[43] *Thorlabs V1550PA Fibre Attenuator Specifications.* `https://www.thorlabs.com/drawings/996a0de59eb4ca1d-29769CB7-C9F7-6187-DDD3E4DA165FDC16/V1550PA-SpecSheet.pdf`, Last Access: 01.03.2023.

[44] *Schäfter+Kirchhoff Series 60FC-SF Fibre Collimator Product Page.* `https://www.sukhamburg.com/products/fiberoptics/fibercoupler/series/60fc-sf.html`, Last Access: 01.03.2023.

[45] *Toptica Photonics CTL Short Specifications.* `https://www.toptica.com/fileadmin/Editors_English/11_brochures_datasheets/03_Short_Info/toptica-CTL-short-info.pdf`, Last Access: 01.03.2023.

[46] *Schäfter+Kirchhoff Series 60FC-F Fibre Collimator Product Page.* `https://www.sukhamburg.com/products/fiberoptics/fibercoupler/series/60fc-f.html`, Last Access: 01.03.2023.

[47] *Thorlabs BS066 Non-Polarising Beam Splitter Cube Product Page.* `https://www.thorlabs.com/newgrouppage9.cfm?objectgroup_id=6208&pn=BS066`, Last Access: 01.03.2023.

[48] *Thorlabs BP145B2 Pellicle Beam Splitter Product Page.* `https://www.thorlabs.com/newgrouppage9.cfm?objectgroup_id=898&pn=BP145B2`, Last Access: 01.03.2023.

[49] *Thorlabs M1050F3 Fibre Coupled LED Specifications.* `https://www.thorlabs.com/drawings/571e0305d4defc6a-2C357CFB-9576-4F42-7E9FF48F837E0F70/M1050F3-SpecSheet.pdf`, Last Access: 01.03.2023.

[50] *Thorlabs M1450F1 Fibre Coupled LED Specifications.* `https://www.thorlabs.com/drawings/1c11e7078e06cc8b-2C49ADA7-FE1B-C760-3692271DF927CEEE/M1450F1-SpecSheet.pdf`, Last Access: 01.03.2023.

[51] *Ocean Insights HL-2000-LL Product Page.* `https://www.oceaninsight.com/products/light-sources/vis-and-nir-light-sources/hl-2000-ll/?qty=1`, Last Access: 01.03.2023.

[52] *Thorlabs BP245B3 Pellicle Beam Splitter Product Page.* `https://www.thorlabs.com/newgrouppage9.cfm?objectgroup_id=898&pn=BP245B3`, Last Access: 01.03.2023.

[53] *Xenics Bobcat 320 Gig-E Product Page.* `https://www.xenics.com/short-wave-infrared-imagers/bobcat-320-series/`, Last Access: 01.03.2023.

[54] *Princeton Instruments NIRvana 640 SWIR Camera Product Page.* `https://www.princetoninstruments.com/products/nirvana-family/nirvana-640`, Last Access: 11.04.2023.

[55] *attocube LT-APO IR 0.81 Specification.* `https://www.attocube.com/downloads/lt-apoir081.pdf`, Last Access: 26.03.2023.

[56] *Andor Shamrock 750 Specification*. `https://andor.oxinst.com/assets/uploads/products/andor/documents/andor-shamrock-750-specifications.pdf`, Last Access: 26.03.2023.

[57] M. Abbarchi, C. Mastrandrea, T. Kuroda, T. Mano, A. Vinattieri, K. Sakoda, and M. Gurioli. "Poissonian statistics of excitonic complexes in quantum dots". In: *Journal of Applied Physics* 106.5 (2009), p. 053504. DOI: `10.1063/1.3197848`. eprint: `https://doi.org/10.1063/1.3197848`. URL: `https://doi.org/10.1063/1.3197848`.

[58] R. Sittig, C. Nawrath, S. Kolatschek, S. Bauer, R. Schaber, J. Huang, P. Vijayan, P. Pruy, S. L. Portalupi, M. Jetter, and P. Michler. "Thin-film InGaAs metamorphic buffer for telecom C-band InAs quantum dots and optical resonators on GaAs platform". In: *Nanophotonics* 11.6 (2022), pp. 1109–1116. DOI: `doi:10.1515/nanoph-2021-0552`. arXiv: `2107.13371 [physics.optics]`. URL: `https://doi.org/10.1515/nanoph-2021-0552`.

[59] W. Sellmeier. "Ueber die durch die Aetherschwingungen erregten Mitschwingungen der Körpertheilchen und deren Rückwirkung auf die ersteren, besonders zur Erklärung der Dispersion und ihrer Anomalien". In: *Annalen der Physik* 223.11 (1872), pp. 386–403. DOI: `https://doi.org/10.1002/andp.18722231105`. URL: `https://onlinelibrary.wiley.com/doi/abs/10.1002/andp.18722231105`.

[60] *Refractive index n of InGaAs*. `https://batop.de/information/n_InGaAs.html`, Last Access: 28.03.2023.

[61] S. Heshmati, H. Taleb, and A. Rahmani. "Complex Sellmeier equation for the refractive index of semiconductors in the opaque region". In: *Optik* 172 (2018), pp. 851–854. ISSN: 0030-4026. DOI: `https://doi.org/10.1016/j.ijleo.2018.07.099`. URL: `https://www.sciencedirect.com/science/article/pii/S0030402618310726`.

[62] P. Kohl. *Implementing the Post Quantum Scheme SABER on RISC-V*. Bachelor's Thesis in Engineering Science at the Chair of Security in Information Technology at the Department of Electrical Engineering of Technical University of Munich. Apr. 2020.